2

The tectonics of Mercury

Thomas R. Watters

Center for Earth and Planetary Studies, National Air and Space Museum, Smithsonian Institution, Washington, DC

and

Francis Nimmo

Department of Earth and Planetary Sciences, University of California, Santa Cruz

Summary

Mercury has a remarkable number of landforms that express widespread deformation of the planet's crustal materials. Deformation on Mercury can be broadly described as either distributed or basin-localized. The distributed deformation on Mercury is dominantly compressional. Crustal shortening is reflected by three landforms, lobate scarps, high-relief ridges, and wrinkle ridges. Lobate scarps are the expression of surface-breaking thrust faults and are widely distributed on Mercury. High-relief ridges are closely related to lobate scarps and appear to be formed by high-angle reverse faults. Wrinkle ridges are landforms that reflect folding and thrust faulting and are found largely in smooth plains material within and exterior to the Caloris basin. The Caloris basin has an array of basin-localized tectonic features. Basin-concentric wrinkle ridges in the interior smooth plains material are very similar to those found in lunar mascon basins. The Caloris basin also has the only clear evidence of broad-scale, extensional deformation. Extension of the interior plains materials is expressed as a complex pattern of basin-radial and basin-concentric graben. The graben crosscut the wrinkle ridges in Caloris, suggesting that they are among the youngest tectonic features on Mercury. The tectonic features have been used to constrain the mechanical and thermal structure of Mercury's crust and lithosphere and to test models for the origin of tectonic stresses. Modeling of lobate scarp thrust faults suggests that the likely depth to the brittle–ductile transition (BDT) is 30 to 40 km. Plausible thermal and mechanical structures for Mercury at the time of faulting suggest an elastic thickness T_e of 25 to 30 km and a heat flux of roughly 30 mWm^{-2}. The thickness of the crust is also constrained to be <140 km. A combination of despinning and thermal contraction may account for equatorial N–S and polar E–W trending lobate scarp thrust faults,

Planetary Tectonics, edited by Thomas R. Watters and Richard A. Schultz. Published by Cambridge University Press. Copyright © Cambridge University Press 2010.

the latter by reactivation of normal faults. However, the observed spatial and temporal distribution of lobate scarps suggests other sources of stress may be important. Stresses resulting from mantle convection may have been significant, while those due to polar wander and buoyancy forces are currently uncertain. Loading in the Caloris basin from infilling of volcanic material likely produced significant compressional stresses that formed the wrinkle ridges. The Caloris graben are probably due to basin exterior loading or lateral flow of the lower crust causing uplift of the basin floor. The absence of widespread extensional faulting outside the Caloris basin is probably due to a compressive stress bias resulting from global thermal contraction. Modeling suggests that T_e during Caloris loading was ~100 km, up to a factor of four larger than estimates of T_e based on lobate scarp thrust faults.

1 Introduction

Mercury is a planet with a number of important characteristics. It is the smallest of the terrestrial planets, not much larger than Earth's moon, and it is the closest planet to the Sun. In spite of its small size, Mercury's mean density is comparable to that of the Earth. This indicates that the proportion of Mercury's core volume to that of its mantle and crust is much larger than the other terrestrial planets. In three flybys during 1974 and 1975, Mariner 10 imaged about 45% of Mercury's surface (~90% of the eastern hemisphere). The Mercury Surface, Environment, Geochemistry, and Ranging (MESSENGER) mission successfully completed the first of three flybys in January 2008 and will become the first spacecraft to orbit Mercury in 2011 (Solomon *et al.*, 2001, 2007, 2008). During the first flyby, images of 21% of the hemisphere unseen by Mariner 10 were obtained by MESSENGER's Mercury Dual Imaging System (MDIS) cameras (Hawkins *et al.*, 2007). Although the summary presented in this chapter is based largely on the Mariner 10 view of Mercury, some of the early new findings from MESSENGER are described.

At first glance, the surface of Mercury looks much like Earth's moon. However, images revealed evidence of tectonism on a much larger scale than exists on the Moon. In fact, the scale of tectonic activity is comparable to that of the larger terrestrial planets. Preserved in Mercury's ancient crust is evidence of post late heavy bombardment crustal deformation. The tectonics of Mercury can be broadly described as either distributed or basin-localized. Distributed deformation on Mercury is dominantly contractional. Three landforms have been found on Mercury that reflect crustal shortening: lobate scarps, wrinkle ridges, and high-relief ridges. Lobate scarps are linear or arcuate features that are asymmetric in cross section, generally consisting of a steeply sloping scarp face and a gently sloping back scarp (Strom *et al.*, 1975; Cordell and Strom, 1977; Dzurisin, 1978; Melosh and McKinnon, 1988; Watters *et al.*, 1998). Where lobate scarps transect impact craters,

there is clear evidence of offsets in wall and floor materials, suggesting they are the expression of surface-breaking thrust faults (Strom *et al.*, 1975; Cordell and Strom, 1977; Melosh and McKinnon, 1988; Watters *et al.*, 1998, 2001).

Wrinkle ridges, in contrast to lobate scarps, are generally more complex morphologic features. They typically consist of a broad, low-relief arch with a narrow superimposed ridge (Strom, 1972; Bryan, 1973; Maxwell *et al.*, 1975). A compressional origin involving a combination of folding and thrust faulting is supported by studies of terrestrial analogues (Plescia and Golombek, 1986; Watters, 1988; Schultz, 2000); however, there is no consensus on the geometry and number of faults or if the faults are surface breaking or non-surface breaking (blind) (see Schultz, 2000; Golombek *et al.*, 2001).

High-relief ridges are a much less common tectonic landform than lobate scarps and wrinkle ridges (Watters *et al.*, 2001). They are generally symmetric in cross section with greater relief than wrinkle ridges. Like lobate scarps, when high-relief ridges transect impact craters they deform the walls and floors. Some high-relief ridges transition into lobate scarps, suggesting that the origins of the two structures are related.

Unlike the other terrestrial planets, evidence of crustal extension on Mercury is nearly absent. The only extensional deformation on Mercury found thus far occurs in the interior plains material of three impact basins (Solomon *et al.*, 2008; Watters *et al.*, 2009a, b). Extension in the Caloris basin is manifested by a complex network of linear and sinuous narrow troughs that are interpreted to be graben (Strom *et al.*, 1975; Melosh and McKinnon, 1988; Watters *et al.*, 2005). No graben are found in the annulus of materials exterior to the Caloris basin.

The array of tectonic features on Mercury provides important clues to the properties and evolution of the planet's crust and lithosphere and its thermal history. The spatial distribution and contractional strain expressed by Mercury's lobate scarps are important to constrain thermal history models and models for the origin of tectonic stresses (see Melosh and McKinnon, 1988). Models for the origin of lobate scarps that emerged from the post Mariner 10 era studies of Mercury are global contraction due to secular cooling of the interior, tidal despinning, a combination of thermal contraction and tidal despinning, and a combination of thermal contraction and stresses related to the formation of the Caloris basin (Strom *et al.*, 1975; Cordell and Strom, 1977; Melosh and Dzurisin, 1978a; Pechmann and Melosh, 1979; Melosh and McKinnon, 1988; Thomas *et al.*, 1988; Dombard and Hauck, 2008).

Interest in Mercury's geologic and tectonic evolution has been rekindled by the new planetary missions to the iron planet. Meantime, new insights into the nature of the tectonic features, their spatial and temporal distribution, the origin of the tectonic stresses, and the mechanical and thermal structure of Mercury's crust and

lithosphere have been gained through the continued analysis of Mariner 10 images. In the following sections, we will describe the current understanding of Mercury's tectonic features and the constraints they provide on existing geophysical and thermal history models.

2 Tectonic features of Mercury

2.1 Topographic data

A major challenge to the identification and analysis of tectonic features on Mercury has been the paucity of topographic data. Topographic data for Mercury have been derived from shadow measurements (Strom *et al.*, 1975; Malin and Dzurisin, 1977; Pike, 1988; Watters, 1988), photoclinometry (Hapke *et al.*, 1975; Mouginis-Mark and Wilson, 1981), point stereoanalysis (Dzurisin, 1978), and Earth-based radar altimetry (Harmon *et al.*, 1986; Harmon and Campbell, 1988; Clark *et al.*, 1988).

Earth-based radar altimetry is an important source of reliable topographic data for Mercury. Altimetry data is determined by transmitting short pulses (12.5 cm or S-band wavelength) and analyzing the radar echoes using the delay-Doppler method (see Harmon *et al.*, 1986). The limitation of Earth-based radar altimetry is that, because of Mercury's 7° orbital inclination, only a band ±12° of the equator can be covered (Harmon *et al.*, 1986; Harmon and Campbell, 1988). Radar altimetry data obtained by the Arecibo antenna between 1978 and 1984 have a resolution cell of 0.15° longitude by 2.5° latitude or 6 km by 100 km and an altitude resolution of ~100 m (Harmon *et al.*, 1986). Data obtained by the Goldstone antenna between 1972 and 1974 have a latitude resolution of ~65 km, a longitude resolution that varies from 10 to 20 km, and an altitude resolution of ~150 m (Clark *et al.*, 1988).

Topographic data with high spatial resolution can be obtained for relatively small landforms with gentle slopes using monoscopic (one dimensional) photoclinometry. The spatial resolution of the topography is only limited by the spatial resolution of the image, and the method is sensitive to small changes in slope (Davis and Soderblom, 1984). Using a photometric function appropriate for Mercury, such as the Lommel-Seeliger/Lambert function (see McEwen, 1991) that describes the photometric properties of the surface, the slope along a defined line is recovered and the relative elevation calculated between adjacent pixels (Davis and Soderblom, 1984; Tanaka and Davis, 1988; Watters and Robinson, 1997). Two-dimensional photoclinometry can be used to generate digital elevation models from an image (Kirk *et al.*, 2003). The method involves generating a topographic surface that approximates the image based on its viewing geometry (Kirk *et al.*, 2003).

Recent efforts to update Mariner 10 camera orientations (Robinson *et al.*, 1999) and improve radiometry (Robinson and Lucey, 1997) have greatly enhanced the

accuracy of topographic data derived from the images. Topographic data for Mercury has been obtained using Mariner 10 stereo images and modern digital stereo methods (Watters *et al.*, 1998, 2001, 2002; Cook and Robinson, 2000; André *et al.*, 2005). The spatial resolution and height accuracy of stereo derived topography is limited by the resolution of the images. Stereo derived topography will be important in obtaining a global topographic map of Mercury. Because MESSENGER will be in an elliptical orbit, the Mercury Laser Altimeter (MLA) will not return ranging data for much of the southern hemisphere (Solomon *et al.*, 2007). The MDIS cameras, however, will obtain global stereo image coverage of Mercury (Hawkins *et al.*, 2007).

2.2 Mapping tectonic features

Tectonic features (i.e., lobate scarps, high-relief ridges, wrinkle ridges, graben) imaged by Mariner 10 have been identified and their locations digitized (Plate 1). The tectonic features were digitized directly from Mariner 10 image mosaics. Where available, topographic data from Mariner 10 stereo coverage and radar altimetry was used to aid in the identification of tectonic landforms (Watters *et al.*, 2004). The stereo topography is particularly useful in identifying tectonic features in areas where the lighting geometry is not optimal for morphologic analysis (incidence angles <45°).

2.3 Lobate scarps

Among the most important discoveries of the Mariner 10 mission was the number and scale of features described by Strom *et al.* (1975) as lobate scarps. The most convincing evidence for a tectonic origin is the expression of a surface-breaking thrust fault in the walls and floors of large impact craters cut by these structures (Figure 2.1). Discovery Rupes (54°S, 37°W), one of the most prominent lobate scarps imaged by Mariner 10, is over 450 km long (Figure 2.1B). New images obtained by MESSENGER confirm that there are lobate scarps in the hemisphere unseen by Mariner 10 (Solomon *et al.*, 2008). One of these scarps, Beagle Rupes (2°S, 259°W), is over 600 km long, greater than the length of Discovery Rupes (Figure 2.2). Sometimes characterized as features unique in the solar system (Thomas *et al.*, 1988), landforms virtually indistinguishable from Mercurian lobate scarps are found in highland intercrater plains on Mars (Watters, 1993, 2003; Watters and Robinson, 1999). Small-scale lobate scarps have also been found in the highlands of the Moon (Howard and Muehlberger, 1973; Lucchitta, 1976; Binder, 1982; Binder and Gunga, 1985; Watters and Johnson, Chapter 4). Reasonable terrestrial analogues to planetary lobate scarps may be Rocky Mountain foreland thrust faults

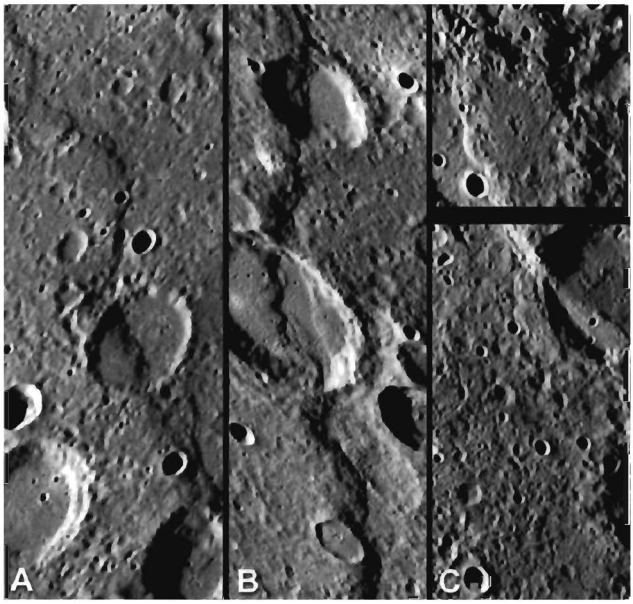

Figure 2.1. Prominent lobate scarps on Mercury. Santa Maria Rupes (A), Discovery Rupes (B), and Vostok Rupes (C) are landforms interpreted to be the surface expressions of thrust faults. The images are approximately 65 km across.

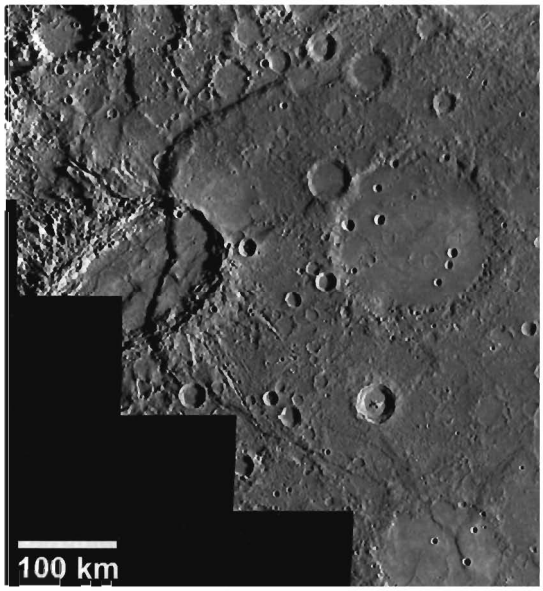

Figure 2.2. Beagle Rupes, a large-scale lobate scarp in the hemisphere unseen by Mariner 10. Beagle is an arcuate lobate scarp over 600 km long, making it one of the longest lobate scarps yet found on Mercury. The walls and floor of the ~220-km diameter, elliptically shaped impact basin named Sveinsdóttir are offsets. The image mosaic was obtained by the MDIS Narrow Angle Camera on the MESSENGER spacecraft.

in Wyoming that cut Precambrian basement and Paleozoic sedimentary sequences (Watters and Robinson, 1999; Watters, 2003).

2.3.1 Topography of lobate scarps

Topographic data for lobate scarps has been obtained from a variety of sources (see Section 2.1). Mariner 10 stereo derived topographic data for Discovery Rupes, Resolution Rupes (63°S, 50°W), and Adventure Rupes (65°S, 63°W) clearly show

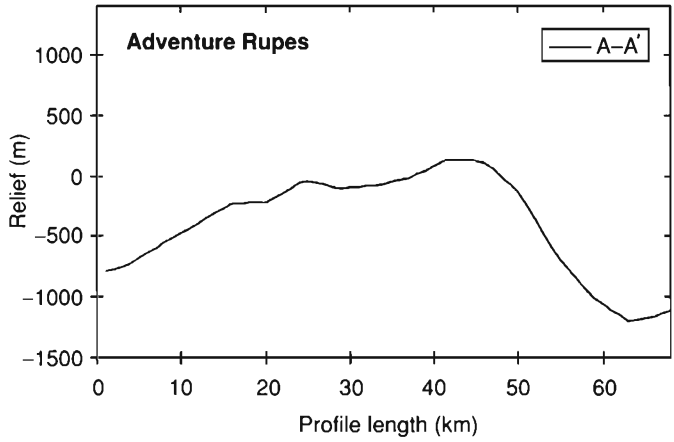

Figure 2.3. Topographic profile across Adventure Rupes obtained from a digital stereo derived DEM (Watters *et al.*, 2001). Profile location is shown in Plate 2. Elevations are relative to the 2439.0 km Mercury radius reference sphere (vertical exaggeration is ~15:1).

the morphology of lobate scarps consists of a relatively steep scarp face and rise and a gently sloping back scarp (Plate 2, Figure 2.3) (Watters *et al.*, 1998, 2001). Discovery Rupes has the greatest relief (~1.5 km) of the lobate scarps measured (Watters *et al.*, 1998, 2001). Adventure Rupes and Resolution Rupes have a maximum relief of ~1.3 km and ~0.9 km respectively.

Photoclinometric data provide an independent check of the accuracy of the stereo derived digital elevation model. Monoscopic photoclinometric profiles across Discovery Rupes compared to stereo derived profiles across the same area of scarp indicate that the difference between the two methods is <10% (<100 m) (Watters *et al.*, 1998). Topographic data for three other prominent lobate scarps, Santa Maria Rupes (3.5°N, 19°W), Endeavour Rupes (38°N, 31°W), and a lobate scarp designated S_V1 (30°N, 28°W) were also obtained using photoclinometry. Of the three, Endeavour Rupes has the greatest relief at ~830 m, followed by Santa Maria Rupes at ~710 m and S_V1 at ~260 m.

Earth-based radar altimetry profiles cross several lobate scarps near the equator. The most prominent is Santa Maria Rupes (Figures 2.1, 2.4). A profile obtained by Arecibo shows that the scarp has a relief of about 700 m (Harmon *et al.*, 1986) (Figure 2.5), in good agreement with the relief estimated from co-located photoclinometric profiles (Watters *et al.*, 1998). The same Arecibo profile indicates that another lobate scarp (4°N, 15°W) to the east of Santa Maria Rupes (designated S_K4) has a relief of ~700 m (Harmon *et al.*, 1986). An Arecibo profile also crosses a lobate scarp (8°N, 13°W) to the northeast of Santa Maria Rupes. This lobate scarp (designated S_K3) has ~470 m of relief.

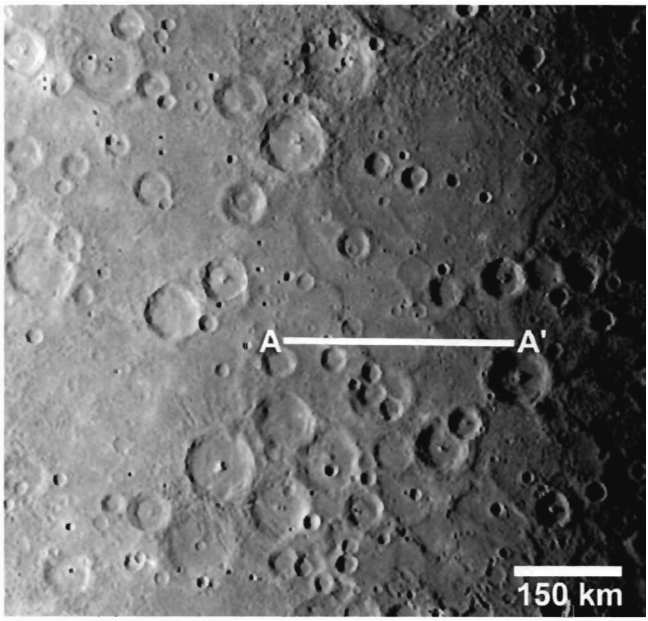

Figure 2.4. Mariner 10 mosaic of part of the Kuiper quadrangle area in the equatorial zone of Mercury. Santa Maria Rupes and other lobate scarps occur in smooth and intercrater plains (see Plate 1). Mosaic covers the region from about 5°S to 15°N and 10°W to 30°W.

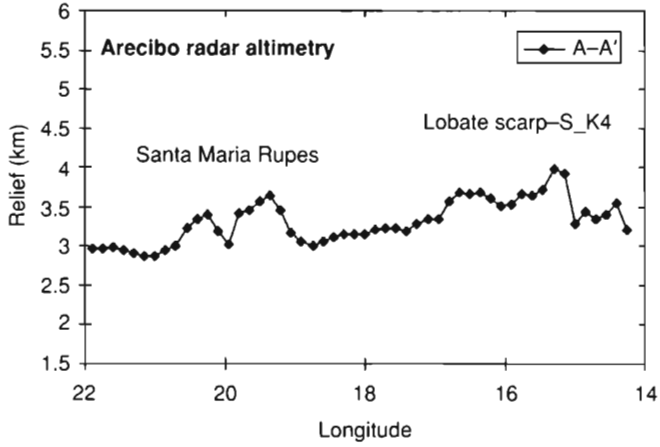

Figure 2.5. Arecibo radar altimetry profile crossing Santa Maria Rupes and another lobate scarp to the east (S_K4). These data are at latitudes of 3.9° to 4.0°N and elevations are relative to the Mercury 2439.0 km radius reference sphere (Harmon *et al.*, 1986). Profile location is shown in Figure 2.4.

The maximum relief of the lobate scarps in the Mariner 10 hemisphere measured with topographic data obtained from digital stereo, monoscopic photoclinometry, and radar altimetry ranges from ~0.26 to 1.5 km ($n = 8$) (Table 2.1). Although based on a small number of measurements, this range in maximum elevation is remarkably consistent with that of lobate scarps on Mars (~0.13 to 1.2 km) (Watters, 2003).

Table 2.1. *Dimensions of lobate scarps imaged by Mariner 10*

Index	Latitude	Longitude	Maximum Relief (m)	Length (km)	D $\theta = 30°$ (m)
DR*	54°S	37°W	1500	457	3000
AR*	65°S	63°W	1300	261	2600
RR*	63°S	50°W	900	127	1800
ER†	38°N	31°W	830	221	1660
SMR‡	5°N	20°W	700	227	1400
S_K4‡	4°N	15°W	700	239	1400
S_K3‡	8°N	13°W	470	163	940
S_V1†	30°N	28°W	260	203	520

The lobate scarps Discovery Rupes (DR), Adventure Rupes (AR), Resolution Rupes (RR), Endeavour Rupes (ER), Santa Maria Rupes (SMR), S_V1, S_K3, and S_K4 are in the digitized database shown in Plate 1. Topographic data was obtained from digital stereo (*), monoscopic photoclinometry (†), and radar altimetry (‡).

2.3.2 Spatial and temporal distribution of lobate scarps

In an analysis of the spatial distribution of lobate scarps imaged by Mariner 10 (Plate 1) the cumulative lengths were plotted in 20° latitude bins, normalized by area (less the portion of the hemisphere not imaged by Mariner 10) (Watters *et al.*, 2004, Fig. 3). The distribution of the mapped lobate scarps does not appear to be uniform in the Mariner 10 hemisphere. It is clear that a relatively large number of lobate scarps occur in the southern hemisphere. In fact, over 50% of the area-normalized cumulative length of the lobate scarps mapped by Watters *et al.* (2004) occurs below 30°S, with the greatest cumulative length between 50°S to 90°S. In the northern hemisphere, there is a gradual decrease in the area-normalized cumulative length from the equator toward higher latitudes, with the exception of the north polar region (70°N to 90°N)(see Watters *et al.*, 2004, Fig. 3).

An inherent weakness of any analysis of the distribution of lobate scarps or other tectonic features on Mercury is the effect of observational bias. Significant observational bias may be caused by variations in lighting geometry (see Cordell and Strom, 1977; Melosh and McKinnon, 1988; Thomas *et al.*, 1988). The incidence angle of the images acquired by Mariner 10 changes from 90° at the terminator to 0° at the subsolar point (0°N, 100°W). This means that only a small percentage of the hemisphere imaged by Mariner 10 has an optimum lighting geometry for the identification of tectonic and other morphologic features. Many of the lobate scarps mapped using Mariner 10 images occur where the incidence angle is >50° (~40° from the terminator), suggesting that the apparent distribution of tectonic features may be significantly biased by lighting geometry. However, the distribution of

the lobate scarps imaged by Mariner 10 is not uniform, even in areas where the incidence angle is >50°. In the intercrater plains between 10°W to 40°W and about 5°S to 30°S (~60° to 90° incidence angle), for example, no lobate scarps are found (Plate 1). It should be noted that lobate scarps are not absent where the incidence angle is <50° and some are found even near the subsolar point (Watters *et al.*, 2004).

Nevertheless, it is clear from an examination of Plate 1 that the number of lobate scarps is much less near the Mariner 10 subsolar point. On approach to Mercury during its first flyby, MESSENGER imaged a portion of the Mariner 10 hemisphere. The location of the terminator was close to the Mariner 10 subsolar longitude. MESSENGER has revealed lobate scarps that were previously undetected in Mariner 10 images of the region (Solomon *et al.*, 2008; Watters *et al.*, 2009a). This clearly demonstrates that Mariner 10-based maps of the lobate scarps are not complete and are strongly influenced by lighting geometry.

To determine the possible effects of lighting geometry on the spatial distribution of the lobate scarps mapped using Mariner 10 images, Watters *et al.* (2004) removed areas of low-incidence angle from the analysis. Lobate scarps within 50° of the subsolar point were eliminated and the corresponding area subtracted from the area-normalized cumulative length plots. Eliminating the area within 50° of the subsolar point (a survey area of ~23% of the surface) does increase the cumulative length of lobate scarps at the equator and in the northern mid-latitudes, but the distribution is far from uniform (Watters *et al.*, 2004, Fig. 3). Thus, the structures identified in Mariner 10 images are not uniformly distributed even in the areas where the illumination geometry is the most favorable (incidence angle >50°) (Watters *et al.*, 2004).

The true distribution of orientations of the lobate scarps imaged by Mariner 10 has been the subject of some debate (Melosh and McKinnon, 1988). Cordell and Strom (1977) first noted a concentration of lobate scarp orientations between ±45° of north. However, they argued that any apparent preferred orientation of the lobate scarps was an artifact of observational bias due to the lighting geometry of the Mariner 10 images. Watters *et al.* (2004) analyzed the distribution of orientations of the mapped lobate scarps by plotting the length-weighted azimuths of the digitized segments and concluded that there is a strong preferred orientation (Watters *et al.*, 2004, Fig. 4). The majority of the segments have orientations that fall between ±50° of north, with the most frequently occurring orientations between N30°W and N40°W and the mean vector at ~N12°E with a circular variance of 0.72 (a uniform distribution has a circular variance of 1). Eliminating the lobate scarps in areas within 50° of the subsolar point does not significantly change the distribution of orientations or the mean vector (Watters *et al.*, 2004, Fig. 4). North of 50°S, the majority of the lobate scarps have NNE, NNW, or N–S orientations. Where the

largest area-normalized cumulative length of lobate scarp segments occur, south of 50°S, the preferred orientations are WNW, ESE, or E–W.

Watters *et al.* (2004) examined the possibility that the orientations of lobate scarps imaged by Mariner 10 are a sample of a larger uniformly distributed population using the Kuiper's Test (Fisher, 1993) for statistical randomness. The Kuiper's *V* statistic, a measure of the largest vertical deviations above and below the diagonal line representing a uniform distribution, for the lobate scarp orientations is large. Based on the deviation of the mapped orientations from a uniform distribution, the hypothesis that the sample orientations are drawn from a uniform distribution was rejected (Watters *et al.*, 2004).

The timing of formation of the lobate scarp thrust faults can be constrained by the age of the materials they deform. The oldest crustal material deformed by lobate scarp thrust faults imaged by Mariner 10 is pre-Tolstojan intercrater plains (see Tanaka *et al.*, Figure 8.1, Chapter 8) emplaced near the end of the period of heavy bombardment (Strom *et al.*, 1975). Younger Tolstojan and Calorian aged smooth plains units (see Tanaka *et al.*, Figure 8.1, Chapter 8) are also deformed by lobate scarps (Plate 1) suggesting that thrust faulting continued after the formation of the Caloris basin and the emplacement of the youngest smooth plains (Strom *et al.*, 1975; Melosh and McKinnon, 1988; Watters *et al.*, 2001, 2004). The absence of lobate scarps in hilly and lineated terrain antipodal to the Caloris basin, where landforms may have been disrupted by basin formation-induced seismic shaking, would suggest that most of the scarps are pre-Caloris in age (Cordell and Strom, 1977), assuming scarps were uniformly distributed. However, a post-Calorian age of formation for many of the lobate scarps imaged by Mariner 10 is suggested by several lines of evidence. One is the crosscutting relations between lobate scarps and impact craters. Lobate scarps often crosscut impact craters (Figure 2.1), some with diameters >60 km. The largest impact feature crosscut by a lobate scarp observed thus far is the ~220-km diameter Sveinsdóttir basin cut by Beagle Rupes (Figure 2.2). Conversely, there are no clear examples of large-diameter impact craters (>40 km in diameter) superimposed on lobate scarps. Further, there is no apparent degradation or partial burial of lobate scarps by Caloris ejecta in the northern hemisphere (Watters *et al.*, 2004). MESSENGER images, however, do show evidence of smaller-diameter impact craters superimposed on lobate scarps (Solomon *et al.*, 2008; Watters *et al.*, 2009a). An example is where a ~30-km diameter impact crater crosscuts the southern segment of Beagle Rupes (Figure 2.2). Another line of evidence is embayment relations between lobate scarps and plains material. Younger Tolstojan and Calorian aged smooth plains overlay intercrater plains (Plate 1), covering ~40% of the hemisphere imaged by Mariner 10 (Spudis and Guest, 1988). In a survey of tectonic features imaged by Mariner 10, no evidence of embayment of lobate scarps by Tolstojan and Calorian smooth plains

materials was found (Watters *et al.*, 2004). The southern segments of Discovery Rupes, for example, deform intercrater plains while the northern segments cut Calorian smooth plains (Plate 1). However, in the hemisphere unseen by Mariner 10, MESSENGER images show the evidence of a lobate scarp embayed by smooth plains material (Solomon *et al.*, 2008; Watters, *et al.*, 2009a). Low-relief ridges in the smooth plains flanking the scarp suggest movement on the thrust fault scarp may have continued after the emplacement of the smooth plains. Thus, these observations suggest that lobate scarp formation developed after the emplacement of the intercrater plains (~4 Ga) and before the end of smooth plains emplacement, continuing after the emplacement of the youngest smooth plains material (Watters *et al.*, 2004; Solomon *et al.*, 2008; Watters *et al.*, 2009a). Some lobate scarps appear to be relatively young and are perhaps the youngest endogenic landforms on Mercury.

2.3.3 Geometry of lobate scarp thrust faults

There is general agreement that Mercury's lobate scarps are the surface expression of thrust faults. However, the fault geometry, fault plane dip, and depth of faulting are unknown. Forward mechanical modeling of lobate scarp thrust faults has helped to constrain the characteristics of these faults on Mercury and Mars (Schultz and Watters, 2001; Watters *et al.*, 2002). Using elastic dislocation modeling, Watters *et al.* (2002) examined the fault geometry, sense of slip, and the amount of displacement D on the thrust fault underlying Discovery Rupes, where the relief on the scarp is the greatest. The greatest relief occurs just south of the Rameau crater (60 km in diameter) where the average relief is ~1.3 km (Watters *et al.*, 2002, Fig. 1). A broad, shallow trough about 40 km wide and several hundred meters deep occurs roughly 90 km west of the base of the scarp. The axis of the trough roughly parallels the strike of the scarp face of Discovery Rupes. The trough is interpreted to be evidence of a trailing syncline, and the distance between it and the surface break defines the cross-strike dimension of the upper plate of the thrust fault (Watters *et al.*, 2002). Other back scarp topographic troughs are associated with Adventure Rupes and an analogous lobate scarp on Mars called Amenthes Rupes (Schultz and Watters, 2001; Watters *et al.*, 2001). In the model, the lower tip of the thrust fault is placed below the trailing syncline and its upper tip at the surface break. The initial amount of slip is estimated from the kinematic offset calculated from the height of the scarp adjacent to the surface break. Mercury's seismogenic lithosphere is approximated by an elastic halfspace with a Young's modulus E of 80 GPa and Poisson's ratio ν of 0.25. The best fits to the topography across Discovery Rupes are for a depth of faulting $T = 35$ to 40 km, a fault dip $\theta = 30°$ to 35°, and $D = 2.2$ km (Watters *et al.*, 2002, Fig. 3). It is possible that other non-planar fault geometries, particularly a listric geometry, could be involved in

the formation of lobate scarps. Elastic dislocation modeling of listric thrust faults, approximated by linear segments with varying dips, has been modeled (Watters *et al.*, 2002; Watters, 2004). None of the listric geometries modeled produce fits to the topographic data as good as the planar geometry.

2.3.4 Displacement–length relationship of lobate scarp thrust faults

Studies of terrestrial faults show that the maximum displacement on a fault D scales with the planimetric length of the fault L (e.g., Walsh and Watterson, 1988; Cowie and Scholz, 1992b; Gillespie *et al.*, 1992; Cartwright *et al.*, 1995) and the relationship holds for planetary faults (Schultz and Fori, 1996; Schultz, 1997, 1999; Schultz *et al.*, Chapter 10; Watters *et al.*, 1998, 2000; Watters and Robinson, 1999; Watters, 2003). It has been proposed that D is related to L by $D = cL^n$, where c is a constant related to material properties and n is estimated to be > 1 (Walsh and Watterson, 1988; Marrett and Allmendinger, 1991; Gillespie *et al.*, 1992). A linear relationship $D = \gamma L$, where γ is a constant determined by rock type and tectonic setting (where $n = 1$, $\gamma = c$) (Cowie and Scholz, 1992b), is supported by studies of faults in populations formed in uniform rock types (Dawers *et al.*, 1993; Clark and Cox, 1996). Evidence also indicates that the scaling relationship between D and L generally holds for all the fault types (i.e., normal, strike-slip, and thrust) in a wide variety of tectonic settings and eight orders of magnitude in length scale (Cowie and Scholz, 1992b). The ratio of displacement to fault length γ for the fault populations analyzed by Cowie and Scholz (1992b) ranges between 10^0 and 10^{-3}. Scatter in the D–L data can arise from several sources, including fault segmentation, uncertainties in fault dip and depth or aspect ratio, interaction with other faults, and ambiguities in determining the maximum value of D along the scarp trace (Cartwright *et al.*, 1995, 1996; Dawers and Anders, 1995; Wojtal, 1996; Schultz, 1999; Schultz *et al.*, Chapter 10).

The amount of displacement on some lobate scarp thrust faults imaged by Mariner 10 has been estimated using a kinematic model that assumes the total slip is a function of the relief of the lobate scarp and the dip of the surface-breaking fault plane. Given the measured relief of the scarp h and the fault plane dip θ, the displacement necessary to restore the topography to a planar surface is given by $D = h/\sin\theta$ (see Wojtal, 1996; Watters *et al.*, 2000). The optimum angle θ at which faulting will occur, the angle for which the differential horizontal stress necessary to initiate faulting is a minimum, is given by $\tan 2\theta = 1/\mu_s$ where μ_s is the coefficient of static friction (see Jaeger and Cook, 1979; Turcotte and Schubert, 2002). Laboratory data on the maximum shear stress to initiate sliding for a given normal stress indicates a range in maximum coefficient of static friction of 0.6 to 0.9 (Byerlee, 1978) corresponding to thrust faults with dips from about 24° to 30° with an optimum $\mu_s = 0.65$ resulting in faults with dips of 28.5° (Scholz, 2002).

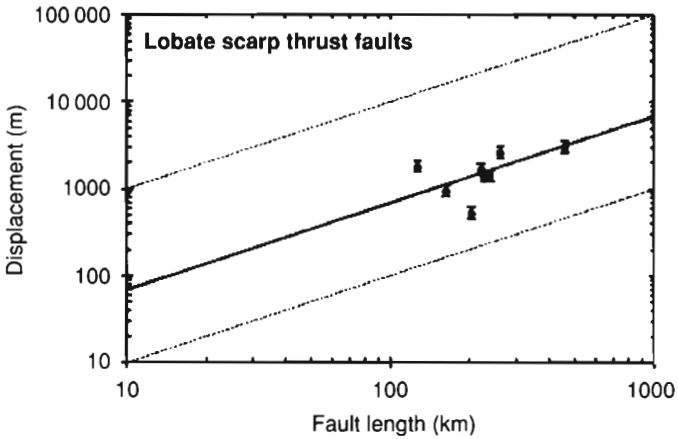

Figure 2.6. Log–log plot of maximum displacement as a function of fault length for eight lobate scarps on Mercury. The ratio γ ($\sim 6.9 \times 10^{-3}$ using estimates of D based on fault plane dips $\theta = 30°$) for the thrust faults (Table 2.1) were obtained by a linear fit to the D–L data with the intercept set to the origin (Cowie and Scholz, 1992b).

The range of expected dips is consistent with field observations of θ for thrust faults that typically range between 20° to 35° (e.g., Jaeger and Cook, 1979; Brewer *et al.*, 1980; Gries, 1983; Stone, 1985). As discussed in the previous section, elastic dislocation modeling of the Discovery Rupes thrust fault and the Amenthes Rupes thrust fault on Mars suggests that the faults dip from 25° to 35° (Schultz and Watters, 2001; Watters *et al.*, 2002).

The estimated displacement on some large-scale lobate scarp thrust faults imaged by Mariner 10 range from 0.52 to 3.0 km, assuming fault plane dips of 30° (Table 2.1), with an average of ~1.7 km ($n = 8$). The amount of displacement on the thrust fault associated with Discovery Rupes is on the order of 2.6 to 3.5 km for θ of 35° and 25° respectively. The value of γ is determined from a linear fit to D–L data for the eight large-scale lobate scarps (Figure 2.6). For a range in θ of 25° to 35°, the corresponding γ is $\sim 6.0 \times 10^{-3}$ to $\sim 8.1 \times 10^{-3}$ and for $\theta = 30°$, $\gamma \cong 6.9 \times 10^{-3}$. These values of γ are consistent with previous estimates for lobate scarps imaged by Mariner 10 (Watters *et al.*, 1998, 2000) and with estimates of γ for lobate scarp thrust faults on Mars (Watters and Robinson, 1997; Watters, 2003).

2.3.5 *Influence of buried basins on lobate scarps*

Many of the known lobate scarps on Mercury are arcuate in plan view (Dzurisin, 1978). Prominent examples are Discovery Rupes, Hero Rupes (~59°S, 172°W), Adventure Rupes, Resolution Rupes (Plate 1) and Beagle Rupes (Figure 2.2). Spudis and Guest (1988) suggest that the population of pre-Tolstojan basins forms

a structural framework that influenced the subsequent geologic evolution of the surface. They mapped 20 pre-Tolstojan multiring basins randomly distributed over the hemisphere imaged by Mariner 10. A number of the proposed remnant rings of the multiring basins have been identified on the basis of circular or arcuate patterns in tectonic features (Pike and Spudis, 1987; Spudis and Guest, 1988). The formation of many of the arcuate lobate scarps may have been influenced by preexisting mechanical discontinuities in the Mercurian crust (Watters *et al.*, 2001, 2004). In an analysis of inferred stresses, where great circles are fit to the perpendiculars of digitized segments of Adventure Rupes, Resolution Rupes, and Discovery Rupes, the maximum concentration of intersection (27% per 1% area) was found to be located at ~48°S, 58°W (Watters *et al.*, 2001, Fig. 7). A possible basin identified by Spudis and Guest (1988) is centered at 43°S, 49°W (Andal-Coleridge basin). The rings of the Andal-Coleridge basin (Spudis and Guest, 1988) are not parallel to the arcuate trend of Adventure and Resolution Rupes and are only subparallel to some northern segments of Discovery Rupes. However, a broad, shallow, roughly circular depression centered at approximately 43°S, 54°W was found in a digital stereo derived regional DEM (Figure 2.7) (Watters *et al.*, 2001). This topographic feature is interpreted to be evidence of another ancient, pre-Tolstojan impact basin, informally named the Bramante-Schubert basin (~550 km in diameter). Segments of Discovery Rupes are roughly concentric to the Bramante-Schubert basin. This may indicate the presence of a ring of the basin that coincides with Discovery Rupes. Another ring of the Bramante-Schubert basin may coincide with two other lobate scarps in the region, Astrolabe Rupes and Mirni Rupes (Watters *et al.*, 2001, Fig. 1). Segments of Adventure Rupes and Resolution Rupes, however, are not strongly concentric to this proposed basin. A topographic depression to the north of Adventure Rupes and Resolution Rupes, roughly centered on Rabelais crater, may indicate the presence of an ancient buried basin (Plate 2, Figure 2.7) that influenced the localization of these structures. It is also possible that the arcuate trend of Adventure and Resolution reflects the influence of an unidentified basin or basin ring not visible in the topography (Watters *et al.*, 2001).

Topographic data suggest that other prominent lobate scarps in the Mariner 10 hemisphere, such as Hero Rupes (~59°S, 172°W) and Fram Rupes (~58°S, 94°W), may be associated with ancient impact basins (Watters *et al.*, 2004). Many of the basins suggested by the topographic data correspond to previously identified pre-Tolstojan multiring basins (Spudis and Guest, 1988). Two other previously unrecognized buried impact basins in the Mariner 10 hemisphere are suggested by opposite-facing arcuate lobate scarps (Plate 1) that ring topographic depressions. They are centered at ~45°S, 142°W and ~10°N, 17°W and are ~300 km in diameter. Thus, mechanical discontinuities introduced by ancient buried impact basins may have influenced the localization of many prominent lobate scarps

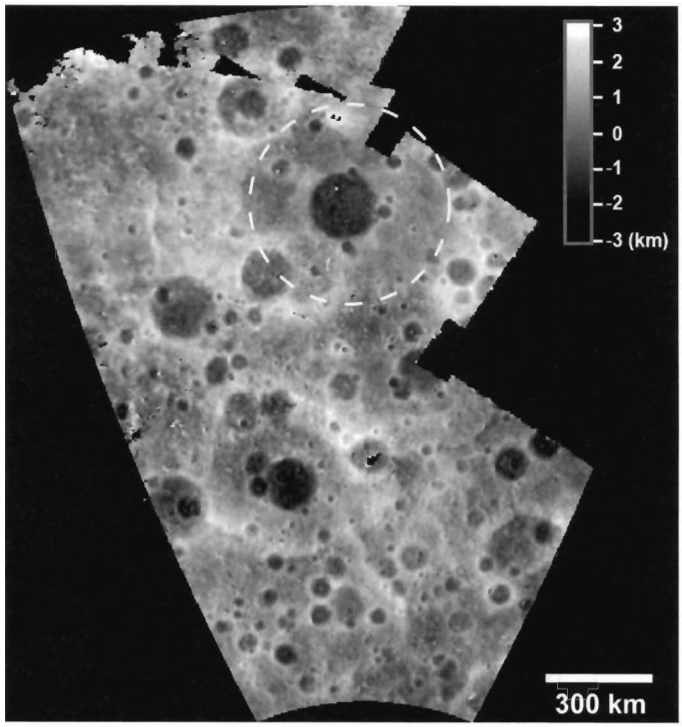

Figure 2.7. Regional-scale DEM of part of the Discovery quadrangle. The dashed line shows the proposed location of an ancient buried impact basin. The DEM covers an area from 25°W to 80°W, 30°S to 75°S and was generated using over 350 individual stereo pairs. Elevations are relative to the 2439.0 km Mercury radius reference sphere.

(Watters *et al.*, 2001, 2004). Many other lobate scarps, however, do not appear to have been influenced by buried impact basins.

2.4 High-relief ridges

High-relief ridges were first described by Dzurisin (1978) as ridges with significant relief found in intercrater plains (also see Melosh and McKinnon, 1988). The morphology and dimension of the high-relief ridges on Mercury is similar to high-relief ridges observed in highland material on Mars (Watters, 1993, Fig. 4a). Although rare in comparison to lobate scarps and wrinkle ridges, eight high-relief ridges imaged by Mariner 10 (Watters *et al.*, 2004) are prominent landforms (Plate 1). Antoniadi Dorsa (30°N, 31°W) is one of the most distinct examples of a high-relief ridge on Mercury (Figure 2.8). It is roughly symmetric in cross section, occurs in intercrater plains, and is ~340 km in length. Antoniadi Dorsa crosscuts an ~85-km diameter impact crater, clearly deforming the crater wall and floor materials.

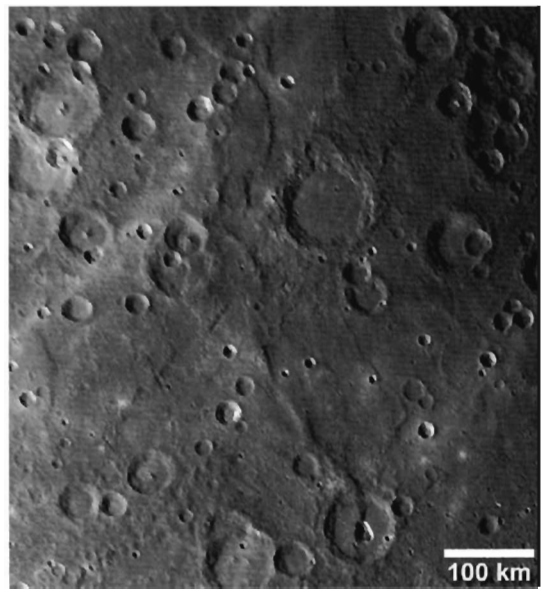

Figure 2.8. Mariner 10 mosaic of the high-relief ridge Antoniadi Dorsa. Antoniadi Dorsa and other high-relief ridges on Mercury are interpreted to be the surface expression of high-angle reverse faulting.

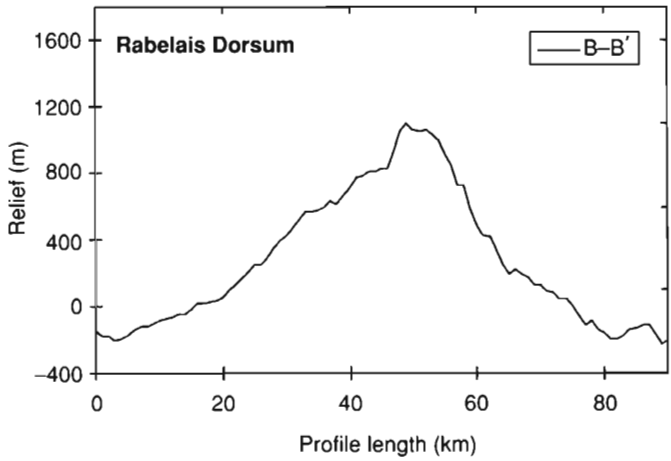

Figure 2.9. Topographic profile across the Rabelais Dorsum high-relief ridge obtained from a digital stereo derived DEM. Rabelais Dorsum is roughly symmetric in cross section with a maximum relief comparable to that of Discovery Rupes. Profile location is shown in Plate 2. Elevations are relative to the 2439.0 km Mercury radius reference sphere (vertical exaggeration is ~40:1).

A high-relief ridge, first described by Dzurisin (1978), is not readily apparent in monoscopic Mariner 10 images. The ridge, informally named Rabelais Dorsum after a nearby crater (Watters *et al.*, 2001), appears as a prominent landform in a Mariner 10 stereo derived DEM of the region (Plate 2). To the north, Rabelais Dorsum crosscuts the Adventure–Resolution Rupes trend (Plate 2). The topographic data show that the northern segment of Rabelais Dorsum is roughly symmetric with a maximum relief of ~1.3 km (Figure 2.9), comparable in relief to that of

Discovery Rupes. Rabelais Dorsum is ~370 km in length, comparable to Antoniadi Dorsa. Landforms described by Malin (1976) as lobate fronts are found on the eastern side of Rabelais Dorsum, superimposed on intercrater plains and the walls and floors of a number of craters with no evidence of significant offset. Malin (1976) suggests that these features are not fault scarps but rather formed through mass movement associated with seismic activity or tectonically controlled volcanic extrusion. To the south, the morphology of the southwest trending segment of the structure transitions from a high-relief ridge to a lobate scarp (Plate 2) (Watters *et al.*, 2001). The lobate scarp segment is ~140 km in length and offsets the walls and floor material of a crosscut impact crater (72°S, 47°W). Another prominent lobate scarp – high-relief ridge transition in the Mariner 10 hemisphere occurs in the intercrater plains south of Tir Planitia (22°S, 178°W) (Plate 1).

The transformation of some high-relief ridges into lobate scarps suggests that the origin of the two structures is related. One possible explanation for the contrast in morphology between high-relief ridges and lobate scarps, if both structures involve reverse faulting, is the dip of the fault plane. High-relief ridges may reflect deformation over high-angle reverse faults ($\theta > 45°$) rather than thrust faults ($\theta < 45°$). If this is the case, the change in morphology may reflect the transition from a high-angle reverse fault underlying the ridge to a low-angle thrust fault underlying the lobate scarp.

High-relief ridges appear to be comparable in age to lobate scarps (Melosh and McKinnon, 1988; Watters *et al.*, 2004). This interpretation is supported by lobate scarp – high-relief ridge transitions and a lack of superimposed large-diameter impact craters. The crosscutting relationship between Rabelais Dorsum and Adventure Rupes and Resolution Rupes, however, suggests that the ridge postdates the formation of these thrust fault scarps. The superposition of Rabelais Dorsum on the trend of these lobate scarps may indicate a local change in the orientation of the stress field over time (Watters *et al.*, 2001).

2.5 Wrinkle ridges

Wrinkle ridges are one of the most ubiquitous tectonic features on the terrestrial planets. Planetary wrinkle ridges are commonly found on topographically smooth material in two physiographic settings, the interior of large impact basins, or broad expansive plains (Watters, 1988). On the Moon, wrinkle ridges are confined to mare material known to be composed of basalt. Wrinkle ridges on Mars and Venus also appear to occur in basalt-like units (Watters, 1988, 1992, 1993). Terrestrial analogues to wrinkle ridges are also found in the continental flood basalts of the Columbia Plateau in the northwestern United States (Plescia and Golombek, 1986; Watters, 1988, 1992). The common association between wrinkle ridges and volcanic plains has led to the widely held conclusion that there is a genetic

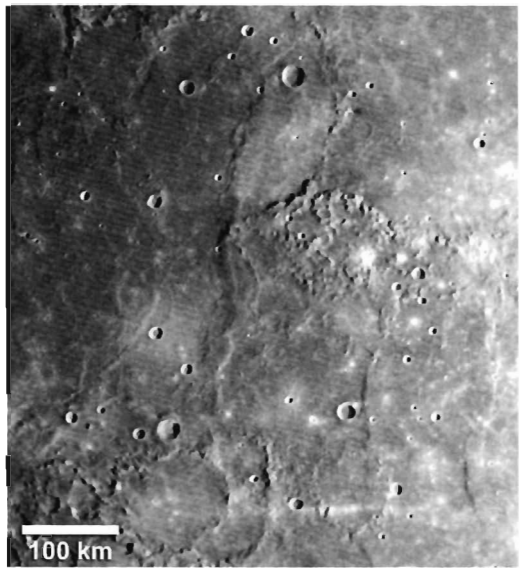

Figure 2.10. Mariner 10 mosaic of the prominent wrinkle ridge, Schiaparelli Dorsum. Schiaparelli Dorsum exhibits the broad arch and superimposed ridge that is typical of planetary wrinkle ridges.

relationship between the two, although this interpretation has been challenged (see Plescia and Golombek, 1986; Schultz, 2000; Watters, 2004).

On Mercury, wrinkle ridges are found in both physiographic settings, basin interior plains and expansive plains outside of basins. By far the largest number of wrinkle ridges in the hemisphere imaged by Mariner 10 occur in the interior smooth plains material of Caloris and the exterior annulus of smooth plains (Plate 1). Some of Mercury's wrinkle ridges would be difficult to distinguish from those in lunar mare or those in ridged plains on Mars. Schiaparelli Dorsum (22°N, 164°W) on the eastern edge of Odin Planitia is a wrinkle ridge that exhibits the typical morphologic elements – a broad, low-relief arch and a superimposed ridge (Figure 2.10). One aspect of planetary wrinkle ridges, however, is that the two morphologic elements that comprise them can occur independently of one another. That is, the relatively narrow ridge and the broad arch may not be superimposed (Watters, 1988). This is the case for many of the wrinkle ridges imaged by Mariner 10 (Strom *et al.*, 1975; Maxwell and Gifford, 1980).

2.5.1 Topography of wrinkle ridges

Little topographic data is available for Mercury's known wrinkle ridges. Estimates of the maximum relief of some wrinkle ridges imaged by Mariner 10 was obtained using poorly constrained shadow measurements (Watters, 1988). Although no Mariner 10 stereo image pairs cover wrinkle ridges, Earth-based radar altimetry profiles do cross the ridged plains of Tir Planitia (Figure 2.11) (Harmon *et al.*, 1986; Harmon and Campbell, 1988; Clark *et al.*, 1988). The relief of seven wrinkle ridges measured in Tir Planitia ranges from 200 to 730 m (Table 2.2). One of these wrinkle ridges (WR_T14), found near the northeastern edge of Tir Planitia (10°N,

Table 2.2. *Dimensions of wrinkle ridges in Tir Planitia*

Index	Latitude	Longitude	Maximum Relief (m)	Length (km)	D $\theta = 30°$ (m)
Wr_T14	10°N	176°W	400	24	800
Wr_T18	9°N	183°W	730	35	1460
Wr_T7	3°N	174°W	440	22	880
Wr_T9	2°S	172°W	200	15	400
Wr_T3	1°S	182°W	370	17	740
Wr_T8	6°N	175°W	250	22	500
Wr_T6	3°N	178°W	340	16	680

The wrinkle ridges are in the digitized database shown in Plate 1. Topographic data was obtained from radar altimetry. Widths were measured from Mariner 10 image mosaics.

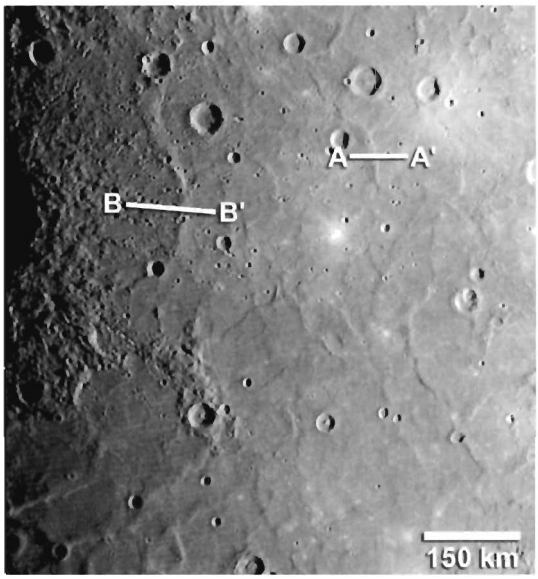

Figure 2.11. Mariner 10 mosaic of part of the Tir quadrangle in the equatorial zone. Wrinkle ridges occur in the smooth plains of Tir Planitia (see Plate 1). Mosaic covers the region from about 5°S to 15°N and 170°W to 190°W.

176°W), has a maximum relief of ~400 m and is ~130 km long (Figure 2.12) (Table 2.2). The altimetry data shows that the ridge is broad and asymmetric. The large width of the ridge, over 30 km, indicates that it is dimensionally more akin to an arch (Watters, 1988). This is the case for all the measured wrinkle ridges in Tir Planitia (Table 2.2). The arch-like structure (WR_T18) near the western edge of Tir Planitia (9°N, 183°W) has the greatest relief of the measured structures at ~730 m. The maximum width of the structure, as measured from Mariner 10 images, is also the largest at ~35 km (Table 2.2). However, the radar altimetry data indicates that this arch is much wider than it appears in images (Figure 2.13). The visible arch is superimposed on a broader landform that is over 50 km wide where the radar altimetry profile crosses it. A Goldstone radar altimetry profile across the

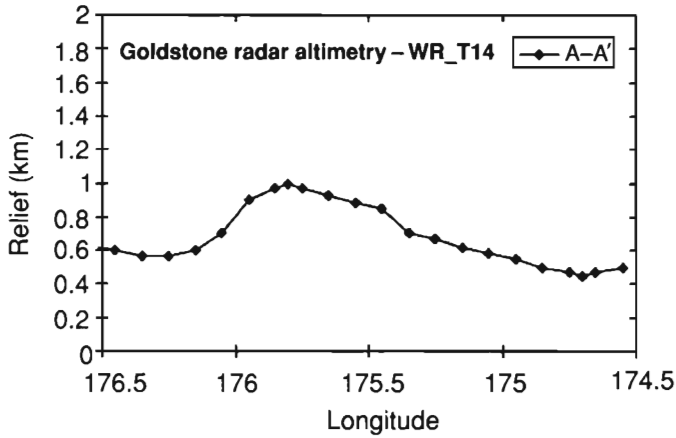

Figure 2.12. Goldstone radar altimetry profile across a wrinkle ridge in Tir Planitia (WR_T14). The width and morphology of the structure indicates that it is an arch. These data are at a latitude of ~9.8°N. Elevations are relative to the Mercury 2439.0 km radius reference sphere (Clark *et al.*, 1988). Profile location is shown in Figure 2.11.

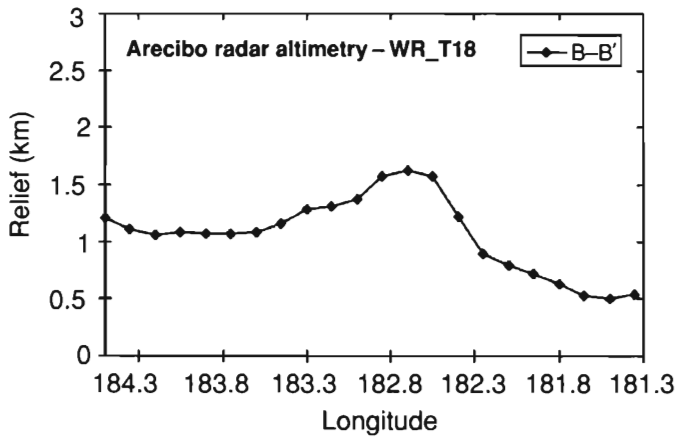

Figure 2.13. Arecibo radar altimetry profile across a high-relief arch-like structure in Tir Planitia (WR_T18). The morphology and high relief of the feature suggests it may be similar to high-relief ridges found in intercrater plains. These data are at a latitude of 8°N and elevations are relative to the Mercury 2439.0-km radius reference sphere (Harmon *et al.*, 1986). Profile location is shown in Figure 2.11.

northern segment of WR_T18 indicates that it may be up to 80 km wide. Although the structure occurs in smooth plains (Plate 1), its large width and great relief make it more akin to a high-relief ridge than to a wrinkle-ridge arch. The high relief of the arches measured using the radar altimetry data, however, is in sharp contrast with the low-relief arches found on the Moon and Mars (see Watters, 1988, 2004).

2.5.2 *Spatial distribution of wrinkle ridges on Caloris exterior plains*

The proximity of the exterior smooth plains to Caloris, and a quick examination of the orientations of the wrinkle ridges (Plate 1), suggests a relationship between the basin and the stresses that formed the wrinkle ridges (Strom *et al.*, 1975; Melosh and McKinnon, 1988; Spudis and Guest, 1988). Many wrinkle ridges on the exterior plains east of Caloris have orientations that appear to be either roughly concentric or radial to the basin (Plate 1). However, many other wrinkle ridges on these smooth plains are not strongly concentric or radial to the Caloris basin. Examining the distribution of orientations of wrinkle ridges in Tir Planitia (~0°N, 180°W), Odin Planitia (~25°N, 170°W), and Suisei Planitia and adjacent plains (~60°N, 160°W) imaged by Mariner 10, suggests there are major trends that could be related to the Caloris basin (Plate 3). In Tir Planitia, the length-weighted azimuths of digitized wrinkle-ridge segments have a vector mean of ~N4°E with a circular variance of 0.62. Although the vector mean is not radial or concentric to Caloris, the trends between N10°W and N40°W are roughly radial, and the trends between N50°E and N60°E are roughly concentric (Plate 3). However, many of the wrinkle ridges in Tir Planitia appear to have been localized by shallow buried impact craters. The vector mean of wrinkle-ridge segments in Odin Planitia is also nearly N–S (~N7°E, circular variance = 0.45). Although this trend and a major trend between N20°E and N30°E are roughly concentric to Caloris, wrinkle ridges form a local concentric pattern in Odin Planitia, possibly reflecting the influence of a buried impact basin. Suisei Planitia has the most consistent trends of the three ridged plains provinces (Plate 3), with a vector mean of ~N38°E (circular variance = 0.33). This trend is perhaps the most clearly radial to the Caloris basin. However, as can be seen in the geologic map of the Mariner 10 hemisphere (Plate 1), this trend also parallels the orientation of the contact between the smooth plains in the Suisei Planitia region and the surrounding intercrater plains. The orientations of many of the wrinkle ridges in Tir, Odin, and Suisei Planitia can be correlated to the gross geometry of smooth plains units that presumably occupy regional-scale lowlands. Earth-based radar altimetry data show that the smooth plains of northern Tir Planitia occur in a broad, roughly N–S trending trough that at its lowest is more than 1 km below the adjacent intercrater plains to the west (Figure 2.14) (Harmon *et al.*, 1986; Harmon and Campbell, 1988). The occurrence of wrinkle ridges in plains units that occupy topographic lows is a characteristic shared by many ridged plains provinces on Mars (e.g., Hesperia Planum) (see Watters, 1993). The presence of wrinkle-ridge rings, wrinkle ridges with semicircular orientations that may have formed over buried impact craters, suggests the ridges are largely the result of subsidence of the plains material (Watters, 1988, 1993). Wrinkle-ridge rings have also been found in MESSENGER images of smooth plains in the hemisphere unseen by Mariner 10 (Head *et al.*, 2008; Watters *et al.*, 2009a). Their presence in volcanic plains on

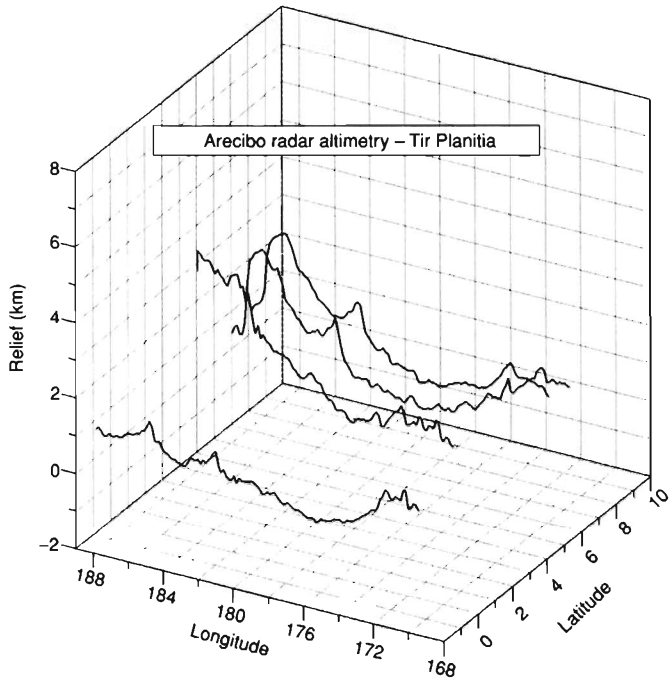

Figure 2.14. Arecibo radar altimetry profiles across Tir Planitia. The topographic data shows that the ridged plains of Tir Planitia occur in a broad trough more than 1 km below the adjacent intercrater plains. Elevations are relative to the Mercury 2439.0 km radius reference sphere (Harmon *et al.*, 1986).

the Moon and Mars along with observed embayment relations supports a volcanic origin for the smooth plains material (Head *et al.*, 2008).

Stresses resulting from subsidence are likely strongly influenced by the geometry of the subsiding plains. Thus, a correlation between the orientation of wrinkle ridges and the geometry of the lowland plains is expected, and stresses resulting from subsidence and the influence of local, shallow, mechanical discontinuities are expected to dominate over influences from the Caloris basin. It is possible, however, that the mechanical discontinuities in the crust introduced by the formation of the Caloris basin are reflected in the trends of wrinkle ridges in the surrounding smooth plains. Wrinkle ridges in Budh Planitia (~20°N, 150°W), to the southeast of Odin Planitia, trend roughly N–S (Plates 1, 3). Budh Planitia has been identified as the location of a possible ancient buried impact basin (Spudis and Guest, 1988). The ridges here, however, are not concentric to Caloris and do not appear to have been influenced by the geometry of the presumed lowland smooth plains. This is also the case for the only other major ridged plains province in the hemisphere imaged by Mariner 10, Borealis Planitia (~75°N, 80°W). Here the wrinkle ridges have predominantly E–W orientations (Plate 1).

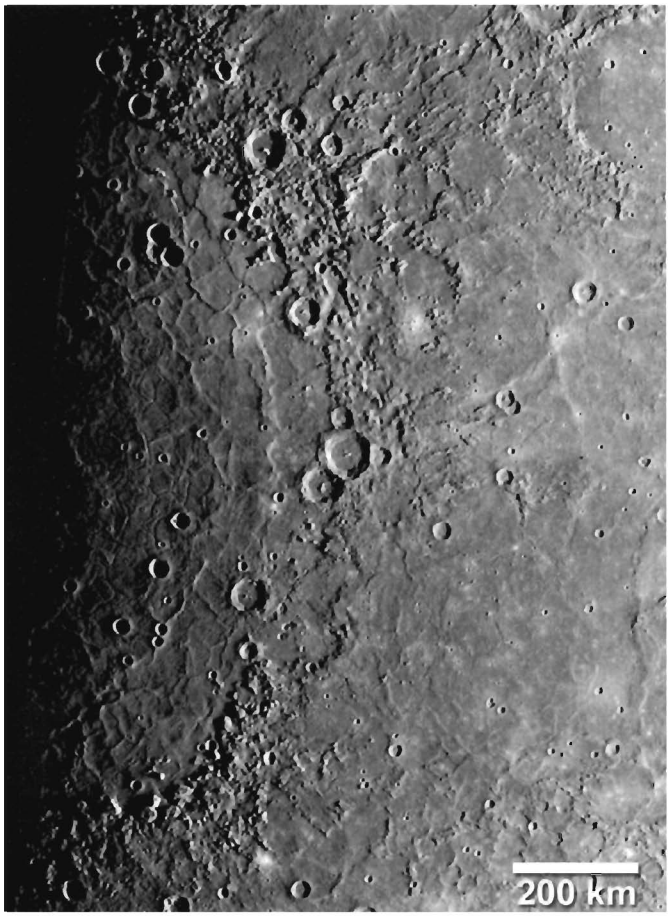

Figure 2.15. Mariner 10 mosaic of the Caloris Basin. The main rim diameter of Caloris is estimated to be ~1300 km. The smooth plains floor material of the imaged side of the Caloris basin has been deformed by both compression and extension.

2.6 Wrinkle ridges in the Caloris basin

The Caloris basin is one of the largest basins in the solar system (Figure 2.15). Based on the portion of the main basin rim imaged by Mariner 10, the diameter of Caloris was estimated to be from ~1300 km (Strom *et al.*, 1975) up to ~1420 km (Maxwell and Gifford, 1980). Less than half of the basin was imaged by Mariner 10 (Figure 2.15). Images obtained by MESSENGER in its first flyby of Mercury cover the entire basin and the diameter of Caloris is now estimated to be about 1550 km (Plate 4) (Murchie *et al.*, 2008). Mariner 10 and MESSENGER images show that wrinkle ridges are found on the interior smooth plains throughout the basin (Plate 4). MESSENGER color data, observed embayment relations, and the discovery of rimless depressions interpreted to be volcanic vents around Caloris support a volcanic origin for the interior smooth plains material (Head *et al.*, 2008; Murchie *et al.*, 2008; Robinson *et al.*, 2008; Watters *et al.*, 2009c).

Wrinkle ridges in Caloris basin are found throughout the interior plains material (Murchie *et al.*, 2008; Watters *et al.*, 2009c). As can be seen in Plate 4, many

more wrinkle ridges are found on the eastern interior plains than on the western plains. This is due, in part, to the much more optimal lighting geometry of the Mariner 10 images of the eastern portion of the basin. The Caloris ridges appear to exhibit only the narrow ridge morphologic element of wrinkle ridges; arches have not been observed (Strom *et al.*, 1975; Maxwell and Gifford, 1980). The widths of Caloris wrinkle ridges imaged by Mariner 10 range from 1 to 12 km, and their maximum relief is estimated at ~500 m (Dzurisin, 1978). This is consistent with the range of widths and maximum relief of wrinkle ridges measured from Mariner 10 images in smooth plains outside of the Caloris basin (Watters, 1988). The location and orientation of wrinkle ridges on the interior plains of Caloris is similar in many ways to lunar maria (Maxwell and Gifford, 1980). These ridges have two predominant orientations, basin concentric and basin radial (Figures 2.15, Plate 4). This pattern is common in lunar mare (Strom, 1972; Bryan, 1973; Maxwell *et al.*, 1975). What is in contrast to lunar mare is the complexity of the pattern of wrinkle ridges of Caloris (Figure 2.15, Plate 4). Crosscutting wrinkle ridges form what has been described as a crude polygonal network (Melosh and McKinnon, 1988). The spacing of parallel to subparallel trending ridges measured in the Mariner 10 portion of the basin ranges from under 10 km to up to 60 km. In some cases, segments of subparallel trending ridges converge and either become subparallel again at a reduced spacing or continue to converge until they merge into a single ridge. A number of wrinkle-ridge rings are also present in the portion of Caloris imaged by Mariner 10, suggesting the influence of shallow buried impact craters.

It has been noted that the basin-concentric wrinkle ridges in the portion of Caloris imaged by Mariner 10 fall along rough arcs in the interior smooth plains (Maxwell and Gifford, 1980; Melosh and McKinnon, 1988). These arcs have been associated with the location of possible interior rings in Caloris. Maxwell and Gifford (1980) found two rings, an innermost ring delineated by a gentle topographic rise at 800 km and a second ring corresponding to ridges at 1060 km diameter. Melosh and McKinnon (1988) determined the diameter of two ridge arcs at 700 km and 1000 km. As in the case of wrinkle ridges in mare basins (see Maxwell *et al.*, 1975), buried basin rings within Caloris may have strongly influenced the localization of the ridges.

2.7 Caloris basin graben

One of the more significant aspects of the tectonics of Mercury is the absence of clear evidence of extension. A network of lineaments may be the subtle expression of extension in the form of a fabric of fractures that make up what has been described as a tectonic grid (Dzurisin, 1978; Melosh and McKinnon, 1988; Thomas, 1997). This grid may reflect ancient lines of weakness in the lithosphere (Melosh and McKinnon, 1988). Clear evidence of extension on Mercury is found in the interior

Figure 2.16. Third-encounter Mariner 10 image mosaic of a portion of the interior plains of Caloris showing extensional troughs that form giant polygons (Mariner 10 images 0529055 and 0529056). One of the longest, continuous troughs in the mosaic (center) forms the boundary of a giant polygon, and cuts the flanks and along the crest of a wrinkle ridge. The maximum width of the mosaic is ~115 km.

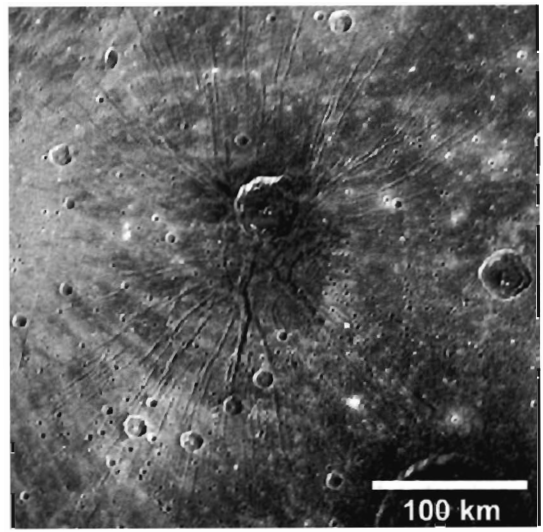

Figure 2.17. Radial graben of Pantheon Fossae in the Caloris basin. The radial graben converge on an area near the center of the basin. The ~40-km diameter impact crater Apollodorus is located in the convergence area. The image mosaic was obtained by the MDIS Narrow Angle Camera on the MESSENGER spacecraft.

plains of the Caloris basin. In addition to the numerous wrinkle ridges, a population of narrow graben near the basin margin was imaged by Mariner 10 (Strom *et al.*, 1975; Dzurisin, 1978). In plan view these graben are highly variable; some segments are linear while others are very sinuous (Figures 2.15, 2.16). The basin-concentric graben account for the dominant trends, however, like the wrinkle ridges there are also basin-radial graben. The basin-concentric and basin-radial graben form polygonal patterns (Plate 4, Figure 2.16) (Dzurisin, 1978; Melosh and McKinnon, 1988; Watters *et al.*, 2005).

MESSENGER has revealed a remarkable new facet of the tectonics of the Caloris basin. A population of radial graben named Pantheon Fossae converge on an area near the center of the basin, close to a ~40-km diameter impact crater (Plate 4, Figure 2.17) (Murchie *et al.*, 2008; Watters *et al.*, 2009c). Other graben near the center of the complex form a polygonal pattern like that seen near the interior margin. MESSENGER images also confirm that basin-concentric graben near the margin extend beyond the Mariner 10 hemisphere, into the western half of the interior plains (Murchie *et al.*, 2008; Watters *et al.*, 2009c). Evidence of extensional faulting outside of Caloris has been found by MESSENGER in the interior plains of the ~250-km diameter Raditladi basin (~27°N, 241°W) (Solomon *et al.*, 2008; Watters *et al.*, 2009a) and in the ~715-km diameter Rembrandt basin (~33°S, 272°W) (Watters *et al.*, 2009b).

The polygonal pattern of the graben in Caloris strongly resembles giant polygons found in polygonal terrains on Mars (Pechmann, 1980; McGill, 1986; Hiesinger and Head, 2000) and Venus (Johnson and Sandwell, 1992; Smrekar *et al.*, 2002). The trough spacing of the largest polygons in the Mariner 10 portion of Caloris is up to 50 km (Figure 2.16), larger than the maximum size of giant polygons

Table 2.3. *Dimensions of troughs/graben in the Caloris basin*

Index	Latitude	Longitude	Maximum Relief (m)	Length (km)	D $\theta = 60°$ (m)
G_S40	27.7°N	184.7°W	220	6.9	254
G_S41	28.8°N	184.9°W	220	9.3	254
G_S42	29.4°N	184.4°W	180	6.8	208
G_S43	27.7°N	185.5°W	180	9.7	208
G_S44	27.5°N	185.1°W	100	6.8	116
G_S45	25.0°N	186.5°W	130	5.6	150
G_S48	28.3°N	185.9°W	160	5.7	185

The troughs/graben are in the digitized database shown in Plate 1. Topographic data were obtained from 2D photoclinometry on a third-encounter Mariner 10 image (0529055). Widths were measured from topographic profiles. The relief of a trough wall measured from the photoclinometrically derived DEM was compared to the relief determined using shadow measurements. They were found to agree by better than ±10 m.

observed on Venus (30 km) (Smrekar *et al.*, 2002), but comparable in scale to some of the largest found in Utopia Planitia on Mars. The mixture of highly sinuous and linear troughs, the wide variation in trough widths and depths, and the wide range in organization of the polygonal pattern are all characteristics strikingly similar to polygon terrain on Mars and Venus.

The widths of graben imaged by Mariner 10 are also highly variable, ranging from hundreds of meters up to ~10 km (Dzurisin, 1978) (Table 2.3). In the wider graben where the interiors are not obscured by shadows, the floors appear to be flat (Strom *et al.*, 1975; Dzurisin, 1978). Topographic data for some of the graben imaged by Mariner 10 have been obtained using 2D photoclinometry (Kirk *et al.*, 2003). Photoclinometry does not produce reliable topographic data in areas obscured by true shadows. Thus, measurements were made only where the majority of the trough floor and walls are without shadows. The topographic data confirm that many of the troughs have relatively flat floors (Watters *et al.*, 2005) (Figure 2.18). The depth of the measured graben in the Mariner 10 portion of the basin varies from ~100 m up to a maximum of ~220 m (Table 2.3) and the walls of the troughs have gentle slopes that are generally between roughly 4° to 6° and do not exceed 10° (Watters *et al.*, 2005). The topographic data show that many graben are flanked on both sides by gently sloping rises (Figure 2.18). These rises or rounded rims vary in relief and are often tens of meters above the surrounding plains.

Basin-radial and basin-concentric graben and wrinkle ridges is a tectonic pattern found in the Caloris basin (Plate 4) and in the newly discovered Rembrandt basin (Watters *et al.*, 2009b, Fig. 4). Similar patterns of tectonic features have not yet been observed in the interior fill of other large impact basins on Mercury, such

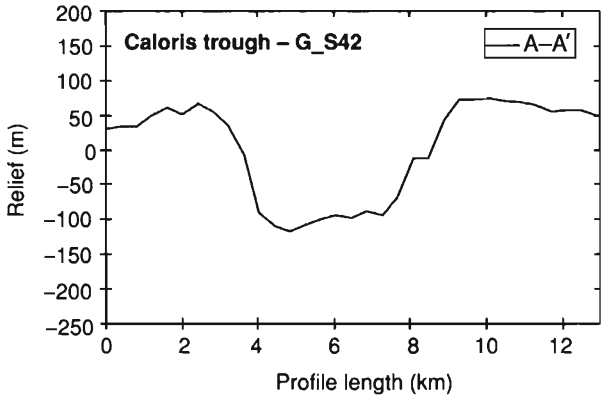

Figure 2.18. Topographic profile across a trough in the Caloris basin. The topographic data show that many of the troughs have relatively flat floors, gently sloping walls, and raised or rounded rims. The profile is from a DEM generated using 2D photoclinometry (see Kirk *et al.*, 2003) on Mariner 10 frame 529055. Profile location is shown in Figure 2.16. Elevations are relative to an arbitrary datum.

as Beethoven and Tolstoj (André *et al.*, 2005). The tectonic patterns in Caloris and Rembrandt are in sharp contrast to lunar mare, where radial and concentric wrinkle ridges occur in mare basalts, and circumferential trough-forming graben occur only near the basin margins (Strom, 1972; Bryan, 1973; Maxwell *et al.*, 1975; Watters and Johnson, Chapter 4). Lunar graben form linear to arcuate troughs with flat floors and steep walls (Baldwin, 1963; McGill, 1971; Golombek, 1979; Watters and Johnson, Chapter 4). The graben are located along basin rims and can cut both mare and basin material (Wilhelms, 1987). Lunar graben often occur in parallel or echelon sets (Golombek, 1979; Wilhelms, 1987). The pattern of wrinkle ridges and graben in some maria are a result of mascon tectonics, where loading from uncompensated basalts causes downward flexure of the lithosphere, resulting in compressional stresses in the interior of the basin that form the wrinkle ridges and extensional stresses on the margins that form arcuate graben (Phillips *et al.*, 1972; Melosh, 1978; Solomon and Head, 1979, 1980; Freed *et al.*, 2001). It is clear that the pattern of compressional and extensional deformation observed in the Caloris and Rembrandt basins is not consistent with lunar-style mascon tectonics (Melosh and Dzurisin, 1978b; Melosh and McKinnon, 1988; Watters *et al.*, 2005; Watters *et al.*, 2009b,c).

An important constraint on the mode and timing of formation of the Caloris graben is the crosscutting relationship between them and the wrinkle ridges. Many of the wrinkle ridges are crosscut by the graben (Figure 2.19). The angle of intersection between the ridges and the crosscutting graben is highly variable. In the Mariner 10 portion of the basin, some graben crosscut wrinkle ridges at nearly orthogonal angles. In other cases, graben roughly parallel wrinkle ridges, cutting

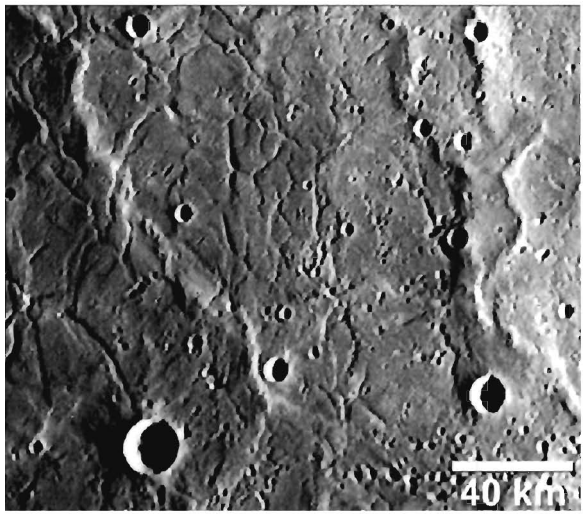

Figure 2.19. Mariner 10 image of troughs and wrinkle ridges on the floor of Caloris. The troughs that form the polygonal terrain crosscut wrinkle ridges suggesting that the troughs postdate the ridges. The areal extent of the troughs is not as great as that of the wrinkle ridges. Mariner 10 frame 106.

their flanks. The crosscutting relations indicate that the graben postdate the wrinkle ridges (Strom *et al.*, 1975; Dzurisin, 1978; Melosh and McKinnon, 1988; Watters *et al.*, 2005; Murchie *et al.*, 2008; Watters *et al.*, 2009c). Thus, compressional deformation of the interior plains materials predates the extension that resulted in the basin-radial and basin-concentric graben. This suggests that initial cooling of the Caloris basin floor material after its emplacement was probably not the cause of the extension, leaving either subsurface heating or uplift of the floor material after the formation of the wrinkle ridges as the explanation (see Section 4.3).

2.8 Summary

The tectonic features on Mercury are dominantly contractional. Lobate scarps, high-relief ridges, and wrinkle ridges are landforms that exhibit crustal shortening. Lobate scarps are the most widely distributed tectonic landform. They are the expression of surface-breaking thrust faults that deform old pre-Tolstojan intercrater plains and relatively young Calorian smooth plains material. Lobate scarps imaged by Mariner 10 are not uniformly distributed spatially and do not exhibit random orientations. They have regional preferred orientations and fault plane dip directions that indicate the influence of regional stresses. Embayment and superposition relations suggest that lobate scarp formation developed after the emplacement of the oldest intercrater plains and continued after the emplacement of the youngest smooth plains material. High-relief ridges, like lobate scarps, are found in intercrater plains and younger smooth plains and appear to be formed by

high-angle reverse faults. Wrinkle ridges are complex landforms that reflect a combination of folding and thrust faulting. They occur exclusively in Calorian smooth plains material. The largest contiguous ridged plains units in the hemisphere imaged by Mariner 10 are in the Caloris exterior annulus. Topographic data indicate that some ridged plains of the eastern annulus occupy lowland areas and suggest that subsidence may have been an important source of compressional stress. Wrinkle ridges are also found in the Caloris interior plains material. The patterns of wrinkle ridges in Caloris are very similar to those found in lunar mascon basins where wrinkle ridges form in response to a super-isostatic load from infilling of mare basalts. Evidence of extension on Mercury is only found in the interior plains of Caloris and two other impact basins. Graben in the interior plains material of Caloris form a complex basin-radial and basin-concentric pattern. Some graben form giant polygons that occur along the interior margin and near the basin center. The complex pattern of graben in the Caloris interior plains material has no analogue in lunar mascons. The graben crosscut the wrinkle ridges and are thus among the youngest tectonic features on Mercury.

3. Mechanical and thermal structure of Mercury's crust and lithosphere

3.1 Introduction

Having discussed the characteristics of tectonic features on Mercury, it is now appropriate to discuss the geophysical implications of these structures. In general, the following sections will concentrate on issues which have changed since the comprehensive reviews of Melosh and McKinnon (1988) and Thomas *et al.* (1988). Few constraints presently exist on the mechanical and thermal structure of Mercury. However, based on the limited data and our experience with other terrestrial planets, Mercury is thought to have an iron core and a silicate mantle (Schubert *et al.*, 1988). Typically, the mantle is overlain by a crust which is compositionally different to the mantle, and is usually more silica-rich and of a lower density. Those parts of the crust and mantle which are relatively cold do not participate in mantle convection over geological timescales and together will be termed the lithosphere. The rigidity of this layer is often expressed as an effective elastic thickness, T_e, which is usually several times smaller than the lithospheric thickness. It is important to recognize that T_e does not give the depth to a particular isotherm or geological feature, though lower elastic thicknesses are usually associated with higher heat fluxes, and that the value of T_e recorded is the *lowest* since deformation occurred. Because the lithosphere usually becomes more rigid over time (due to cooling), the values of T_e estimated are generally relevant to the period of deformation and not the present day.

The heat flux or temperature gradient also determines the depth to the brittle–ductile transition (BDT). Above this level, deformation is typically accommodated by faulting (earthquakes), while below this level, it is accommodated in a ductile

(aseismic) fashion. Because both the BDT depth or seismogenic thickness and elastic thickness are controlled by heat flux, on Earth there is generally a good correlation between these two quantities (e.g., Maggi *et al.*, 2000).

Mariner 10 flyby data give a density structure for Mercury consistent with a mantle approximately 600 km thick (Schubert *et al.*, 1988). Surface reflectance spectra (Vilas, 1988; Sprague *et al.*, 1997) and Mariner 10 color observations (Robinson and Lucey, 1997) suggested a surface composition deficient in opaque mineral and possibly similar to that of the lunar highlands crust. MESSENGER color observations, however, suggest Mercury's crust is largely volcanic in origin, with significant compositional heterogeneities, and that a low-reflectance component is enriched in iron- and titanium-bearing opaque materials (Robinson *et al.*, 2008; Denevi *et al.*, 2009). Thus, the existence of a crust on Mercury is very likely. However, the thickness of this crust is poorly constrained.

Mercury has a significant topographic equatorial ellipticity, based on radar ranging data (Anderson *et al.*, 1996). However, the equivalent gravity coefficient is much smaller than the value which would be inferred from this ellipticity, suggesting that the long-wavelength topography is compensated. The apparent compensation depth is 200 ± 100 km (Anderson *et al.*, 1996), which is interpreted to be the crustal thickness. On other planets, similar analyses at shorter wavelengths sometimes yield comparable apparent depths of compensation, which are usually interpreted as reflecting lithospheric thicknesses (e.g., Smrekar and Phillips, 1991). It will be argued below, on the basis of geological observations, that crustal thicknesses on Mercury are likely to be at or less than the bottom of the range proposed by Anderson *et al.* (1996).

On Earth, the base of the lithosphere is often defined as a particular isotherm, usually around 1100 to 1300 K (e.g., Parsons and McKenzie, 1978; Breuer *et al.*, 1993). The justification for this approach is that geological materials have strongly temperature-dependent viscosity, and thus below a particular temperature they will not participate in convective motions (e.g., Solomatov, 1995). Here, we will generally assume a base lithosphere temperature of 1400 K, both to be conservative and to take into account the likely dryness of the lithosphere on Mercury.

3.2 Thermal structure

The lobate scarps are perhaps the most distinctive class of tectonic feature on Mercury. Earlier in this chapter (subsection 2.3.4) it was shown that stereo topography across lobate scarps can be used to infer the approximate depth of faulting (30 to 40 km). On Earth, large earthquakes rupture all the way to the base of the seismogenic zone. Hence, the inferred vertical extent of the faults on Mercury places a crude constraint on the BDT depth and thus the thermal structure of

Mercury at the time of faulting (Watters *et al.*, 2002). This simple observation has been used to make several inferences about the thermal and mechanical properties of the lithosphere at the time that faulting occurred.

Watters *et al.* (2002) assumed that the BDT depth was in the range 300 to 600 °C and inferred a heat flux at the time of faulting of 10 to 43 mWm^{-2}. They assumed a thermal gradient in which little heat was produced within the crust. Nimmo and Watters (2004) obtained a subcrustal heat flux of 30 to 50 mWm^{-2} if little heat production took place within the crust, but obtained a range of 0 to 45 mWm^{-2} if crustal heat production rates were similar to lunar highland values. In either case, the total heat flux required to produce the correct BDT depth exceeded the likely total radiogenic heat flux by about 10 mWm^{-2}. A heat flux in excess of the heat production is characteristic of planets during their early thermal evolution (see Sections 5.2 and 5.5).

Given these approximate bounds on heat flux at the time of deformation, it is then possible to place constraints on the thickness of the crust. Topography which is supported by variations in crustal thickness decays with time as the lower part of the crust flows laterally; the rate of decay increases with crustal thickness and temperature (e.g., Nimmo and Stevenson, 2001). Based on the survival of Mercurian topography over 4 Gyr, and using a rheology appropriate to dry plagioclase and heat fluxes similar to those derived above, Nimmo (2002) concluded that the crust was <200 km thick. A different approach was presented by Nimmo and Watters (2004), who argued that the joint requirements of a 30- to 40-km BDT depth and an absence of melting at the base of the crust constrained the crustal thickness to be <140 km. Thicker crusts either produced BDT thicknesses which were too shallow or resulted in widespread crustal melting. These constraints, although still crude, are consistent with the geodetic estimate of Anderson *et al.* (1996) of 100 to 300 km.

Using the approach of Nimmo and Watters (2004), two hypothetical temperature profiles for Mercury which produce the correct BDT depth are shown in Figure 2.20A. Both cases have a relatively thin crust (60 km). The lithospheric thickness varies depending on the balance between heat production within the crust and heat flow into the base of the crust, but in either case is relatively thin (81 to 109 km). Crusts which were much thicker would result in the crustal thickness exceeding the lithospheric thickness. Figure 2.20B shows the resulting stress–depth distribution and demonstrates that the bulk of the strength of the lithosphere arises from the brittle portion.

3.3 Elastic thickness

The bounds on heat flux also allow constraints to be placed on the rigidity or elastic thickness T_e of the lithosphere. Nimmo and Watters (2004) used the

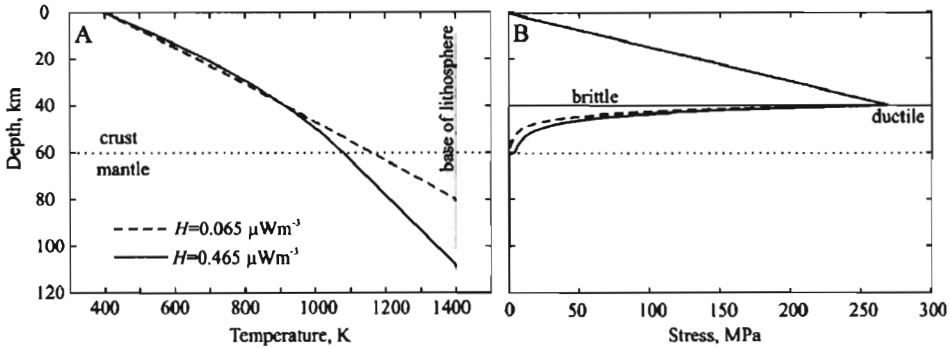

Figure 2.20. Hypothetical Mercury temperature profiles resulting in a BDT depth of 40 km, both with crustal thickness 60 km. Solid line has crustal heat generation rate $H = 0.465\ \mu\text{Wm}^{-3}$ and subcrustal heat flux $F_b = 20\ \text{mWm}^{-2}$; dashed line has $H = 0.065\ \mu\text{Wm}^{-3}$ and $F_b = 36\ \text{mWm}^{-2}$. Lithospheric thicknesses (defined as depth to 1400 K isotherm) are 109 km and 81 km, respectively. (B) Stress–depth profiles for temperature profiles shown in (A). Crustal rheology is dry plagioclase in the dislocation creep regime, mantle rheology is dry olivine. Strain rate is $10^{-17}\ \text{s}^{-1}$, grain size 1 mm. For a curvature of $5 \times 10^{-7}\ \text{m}^{-1}$, the effective elastic thicknesses are 33 km and 25 km, respectively. Method and other parameters are given in Nimmo and Watters (2004).

yield-strength envelope approach of McNutt (1984) and showed that for the kind of stress–depth profiles shown in Figure 2.20B and for typical curvatures associated with the large-scale lobate scarps, T_e was typically about 75% of the BDT depth. Thus, the effective elastic thickness at the time of faulting is predicted to have been 25 to 30 km. The value of T_e at the present day on Mercury is undoubtedly larger than this value; however, the value recorded is the lowest since the deformation occurred. Thus, only the youngest deformation features on Mercury are likely to provide estimates of T_e relevant to the planet's present-day state. The issue of spatial and temporal variations in T_e is discussed further below (Section 5.2).

3.4 Fault properties

Both the depth to the BDT and the thickness of the crust are likely a factor >2 larger than typical terrestrial continental values. However, the gravitational acceleration on Mercury is only about 38% of the Earth's. Thus, the overburden pressure at the base of the BDT on Mercury is comparable to the terrestrial value, about 300 MPa (Figure 2.20B). Despite the large overburden pressures acting to prevent fault motion, terrestrial faults slip under low differential stresses (of order 10 MPa), probably because the presence of pore fluids reduces the overburden pressure and can lubricate fault planes (e.g., Rice, 1992). No such lubrication is likely on Mercury, which may help to explain why large-scale tectonic deformation is relatively rare. However, the fact that faults formed and accumulated significant

displacements suggests that stresses could be quite large; potential sources of stress are discussed in Section 5.4 below.

Observations of lobate scarps may provide insight into fault properties on Mercury. A limited dataset ($n = 8$) of lobate scarps suggests that the maximum *D–L* ratio γ is $6.9 \pm 1 \times 10^{-3}$ (subsection 2.3.5). It has been argued that γ contains information about the mechanical properties of the rock and the regional stresses (Cowie and Scholz, 1992a). Specifically, by adopting a model which takes into account inelastic deformation near the fault tip, it can be shown that

$$\gamma = \frac{(1 - \nu)(\sigma_o - \sigma_f)}{\mu} f(\sigma_a, \sigma_o, \sigma_f), \tag{2.1}$$

where ν is Poisson's ratio, σ_o is the shear strength of the rock, σ_f is the residual frictional stress on the fault, μ is the shear modulus, and $f(\sigma_a, \sigma_o, \sigma_f)$ is a factor of order 1 which increases as the remote stress σ_a increases.

Terrestrial faults show a wide variety of scatter in γ (e.g., Cartwright *et al.*, 1995; Dawers and Anders, 1995). Thus, equation (2.1) is undoubtedly a simplification of a more complex mechanical problem (see, for example, Cowie and Shipton, 1998; Schultz and Fossen, 2002; Schultz *et al.*, Chapter 10). Nonetheless, thrust faults in the Canadian Rocky Mountains ($n = 29$), a likely terrestrial analogue to lobate scarps, have a γ of 8×10^{-2} (Watters *et al.*, 2000). This value of γ is significantly higher than the Mercury lobate scarps. Similarly, the value of γ obtained for Mercury is towards the low end of the range of values compiled by Cowie and Scholz (1992b). Equation (2.1) shows that a likely explanation for the low value of γ is that either μ or σ_f are larger on Mercury than on Earth, or that σ_o is smaller.

It is unlikely that σ_o is smaller than the terrestrial value, since dry rocks are typically stronger than wet rocks. Although μ might be higher on Mercury than on Earth, it is perhaps more likely that σ_f, the residual frictional stress on the fault, is larger. As argued above, terrestrial faults on Earth are weak because of the presence of water; on Mercury, there is no water available to lubricate the fault and reduce σ_f. Thus, a natural explanation for the low value of γ found for the Mercury lobate scarps is the high friction on faults on Mercury, due to the absence of water. Faults on Venus are also thought to be strong for similar reasons (Foster and Nimmo, 1996).

3.5 Summary

The observed and modeled characteristics of lobate scarp thrust faults have allowed the likely depth to the BDT transition (30 to 40 km) to be inferred. This BDT depth places constraints on the thermal structure at the time of faulting and also implies an elastic thickness of 25 to 30 km. The thickness of the crust at the time of faulting was probably < 140 km, and the inferred heat fluxes exceed the likely amount from

radiogenic sources 4 Ga. Plausible thermal and mechanical structures for Mercury 4 Ga are shown in Figure 2.20. Faults on Mercury are probably significantly stronger than their terrestrial counterparts, owing to the absence of water.

4. Mechanical and thermal structure of the Caloris basin

The tectonic features in the Caloris basin are among the most complex and interesting on Mercury, consisting of structures that express at least two distinct episodes of deformation (see Sections 2.6, 2.7). The interior of Caloris consists of early compressional wrinkle ridges, cut by later extensional troughs. Both tectonic landforms have implications for the local crustal structure of the basin.

4.1 Caloris wrinkle ridges and the brittle–ductile transition depth

Wrinkle ridges have been recognized on all the terrestrial planets (see Sections 2.5, 2.6). It has long been thought that the characteristic spacing of these features provides information about the thickness of the layer in which deformation occurs. However, wrinkle ridge spacing in ridged plains on Mars of ~30 km have been interpreted as indicating both thin (few km) and thick (few tens of kilometers) layers (Zuber and Aist, 1990; Watters, 1991). This is because ridge spacing can be accounted for with layer instability models where the lithosphere is free to deform (Zuber and Aist, 1990) or where the lithosphere is assumed to be rigid (Watters, 1991).

In a recent series of papers, Montesi and Zuber (2003a,b) have developed a model in which strain localization occurs in response to compression of a material which is strongly strain-weakening. The characteristic spacing of the zones of localization depends on the depth to which the localization extends; that is, the BDT depth. The model parameters are not easy to relate to measurable properties of rock specimens. Nonetheless, for likely parameters Montesi and Zuber (2003a,b) concluded that a typical ratio of ridge spacing to BDT depth was in the range of 0.25 to 1.15. Note that in this formulation, the BDT depth can exceed the ridge spacing, while in conventional buckling theory the buckling wavelength generally significantly exceeds the layer depth.

Wrinkle ridge spacing in the interior of the Caloris basin varies greatly from under 10 km to over 60 km with a median of 33 km ($n = 32$). The results of Montesi and Zuber (2003a,b) thus imply a minimum BDT thickness of 25 km and an upper bound of 120 km. Note that this estimate assumes that any rheological layering at the base of the basin infill does not have a significant effect. As noted above, the importance of the BDT depth is that it places constraints on both the thermal structure and effective elastic thickness of the lithosphere. Although the

uncertainties are so large that further investigation is premature, it is nonetheless striking that the BDT depth range thus obtained is consistent with that inferred for the lobate scarps (subsection 2.3.4). It is important to note that ridge spacing in the Caloris basin may have been influenced by shallow buried impact craters and possibly by buried interior basin rings (see Section 2.6).

As Watters *et al.* (2000) point out, generating sufficient horizontal stresses to achieve motion on low-angle thrust faults is non-trivial. For a stress of 100 MPa, thrust faulting is restricted to depths shallower than about 10 km. Since stresses of this order are likely to have been present on Mercury (Section 5.4), invoking thrust faults extending to a few tens of kilometers is probably not unreasonable. Nonetheless, the possibility remains that wrinkle ridges are relatively shallow-rooted structures.

Wrinkle ridges are interpreted to be the surface expressions of folding and thrust faulting (e.g., Watters, 1988, 2004; Golombek *et al.*, 1991; Schultz, 2000). Assuming that the bulk of the strain is due to displacement on blind thrust faults, it is possible to estimate the regional strain if the *D*–*L* ratio γ for wrinkle ridges is known. The estimated displacement on Mercury's wrinkle ridge thrust faults range from 0.4 to 1.5 km with an average of ~0.8 km ($n = 7$), assuming fault plane dips of 30° (Table 2.2). A linear fit to the *D*–*L* data for the wrinkle ridges yields a value of $\gamma \cong 3.5 \times 10^{-3}$ for $\theta = 30°$. The Yakima folds in the Columbia Plateau basalts, which are a likely terrestrial analogue to wrinkle ridges (Watters, 1988, 1992), show a somewhat larger γ of $2.9 \pm 1.0 \times 10^{-2}$ (Mege and Reidel, 2001). This difference likely reflects the much larger accumulated shortening on the anticlinal ridges of the Columbia Plateau (Reidel, 1984) compared to planetary wrinkle ridges (Watters, 1988). The strain can be calculated by summing the lengths of the digitized wrinkle ridges within the Caloris basin (Plate 4) if the *D*–*L* relationship of the fault population is known (Scholz and Cowie, 1990; Cowie *et al.*, 1993). The strain for large faults ($L \geq$ the maximum depth of faulting) is given by

$$\varepsilon = \frac{\cos(\theta)}{A} \sum_{k=1}^{n} D_k L_k, \tag{2.2}$$

where θ is the fault plane dip, A is the survey area, n is the total number of faults, and $D = \gamma L$ (Cowie *et al.*, 1993). The compressional strain over the entire area of the basin (~1.89×10^6 km^2) is roughly 0.07% (Watters *et al.*, 2009c). More sophisticated models which take into account inelastic effects will reduce the calculated strain somewhat (Mege and Riedel, 2001).

On Earth, fault length distributions can be either power-law or exponential (e.g., Hardacre and Cowie, 2003). For wrinkle ridges <150 km long, the distribution within Caloris is clearly exponential, with a slope of 0.03 km^{-1}. Such exponential

fault distributions are also found at terrestrial mid-ocean ridges (Cowie *et al.*, 1993). Unfortunately, even on Earth, the significance of these distributions is unclear. For instance, although in some cases it appears that the thickness of the brittle layer can have an effect on fault population statistics (e.g., Ackermann *et al.*, 2001), numerical models suggest that such statistics depend in a complex fashion on the amount of strain, the degree of fault linkage and the amount of fault nucleation (Hardacre and Cowie, 2003). The significance of the Caloris wrinkle-ridge length distribution is thus not clear at the present time.

4.2 Strain and depth of faulting of extensional troughs

The extensional troughs in the Caloris basin, postdate the wrinkle ridges, are more closely spaced than the wrinkle ridges, and form polygonal patterns. As with the lobate scarp and wrinkle-ridge thrust faults, the regional strain can be estimated if the *D–L* ratio of the trough forming graben is known. The slope of the measured trough walls does not exceed 10°, which is much lower than likely fault plane dips on the bounding normal faults (>45°). The low trough wall slopes are presumably due to mass wasting, probably related to impact processes (Watters *et al.*, 2005). Assuming initial fault plane dips of ~60°, the estimated displacement on the normal faults ranges from 0.11 to 0.25 km with an average of ~0.2 km ($n = 7$) (Table 2.3). A linear fit to the *D–L* data for the graben yields a value of $\gamma \cong 2.2 \times 10^{-3}$ ($\theta = 60°$). Determination of γ is complicated by the variability of the trough width and the combination of highly sinuous and linear trough segments. The linkage relationship between fault segments forming the polygonal pattern is also not obvious. It is assumed that each trough segment is independent. Using Equation (2.2), the extensional strain over the total area of the Caloris basin is roughly 0.08% (Watters *et al.*, 2009c), comparable to the estimated contractional strain due to the wrinkle ridges.

The depth of trough-forming faults is not well constrained, but the relatively close spacing of the troughs and their narrow widths suggest relatively shallow-rooted faulting. If the fault planes actually intersect, they will do so at a depth of about 2 to 5 km. Although the faults may penetrate below the 2 to 5 km intersection depth, this depth of faulting is either comparable to or smaller than that estimated from the wrinkle ridges (see Section 4.1). The closer average spacing of the troughs compared to the wrinkle ridges suggests that the trough-forming faults are confined to the basin floor material.

It may also be possible to constrain the depth of faulting using the relationship between the spacing of the polygonal graben and the thickness of the deformed floor material. Based on analysis of the variation in the maximum depth of failure with temperature gradient, Johnson and Sandwell (1992) estimated that the range

in ratio of polygon width to thickness on Venus varies from 0.5 to 16. They also noted that the ratio of the dominant wavelength of deformation to layer thickness in thin layers under uniaxial compression or tension is about 4, roughly the same order of magnitude. The range in widths of the most pronounced Caloris polygons varies greatly from ~7 to 50 km, with a median of 14 km ($n = 15$). A ratio of 4 corresponds to a range in depth of 1.8 to 12.5 km, in good agreement with the above estimate based on fault geometry.

4.3 Caloris loading history

The fact that Caloris experienced compression followed by extension places constraints on its geological history (e.g., McKinnon, 1980; Melosh and McKinnon, 1988; Thomas *et al.*, 1988). Some insight may be gained by considering the likely events following a large impact. The initial impact creates a transient cavity which is modified over the course of a few minutes by collapse (Melosh, 1989). The vaporization and excavation of crustal material results in the crater being initially out of isostatic equilibrium; vertical mantle uplift results, with a timescale probably comparable to the $\sim 10^3$ year timescale characteristic of glacial rebound on Earth. At the end of this process, the basin will overlie thinned crust and be in isostatic equilibrium. The energy delivered by the impactor will result in raised temperatures surrounding the basin, which will decay over a timescale set by diffusion (at least a few Myr for Caloris).

4.3.1 Wrinkle ridges

On the Moon, mare volcanism flooded the nearside basins (Solomon and Head, 1979). Geological mapping and crater counting of the deposits in the Caloris basin suggest that they are probably volcanic in origin and postdate the formation of the basin (Spudis and Guest, 1988). Unfortunately, the thickness of the deposits is not well constrained (see Section 4.2) and the topography of the basin is currently unknown. If later volcanism does occur, the original floor of the basin will subside, but depending on the rigidity of the basin and the density of the fill, its new surface may be either higher or lower than the original level. Subsidence in response to loading can lead to compression of the basin-interior floor material. Melosh and McKinnon (1988) concluded that subsidence was the most likely cause of the Caloris wrinkle ridges.

If the basin maintains elastic strength, then the maximum strain ε caused by sagging or uplifting of the basin center by an amount w_0 is given by

$$\varepsilon \approx w_0 \left(\frac{2\pi}{\lambda}\right)^2 \frac{T_e}{2}, \tag{2.3}$$

where λ is the basin width ($\sim$1550 km for Caloris). An inferred compressive strain of 0.07% implied by the wrinkle ridges imaged by Mariner 10 and MESSENGER requires $w_0 \sim 3$ km for $T_e = 30$ km, $w_0 \sim 1$ km for $T_e = 100$ km, and $w_0 < 1$ km for $T_e = 150$ km. Alternatively, subsidence of the basin floor due to surface loading may lead to compressional thermal stresses at depth. A compressional strain of $\sim$0.07% requires a temperature increase of 25 K. For the likely heat fluxes of 30 to 50 mWm^{-2}, such a temperature increase requires a depth increase of 1.5 to 2.5 km.

Cooling of an initially hot layer can also lead to compressional stresses. Parmentier and Haxby (1986) showed that a cooling layer which is free to contract horizontally will develop compressional stresses near the surface and tensional stresses at depth. We think it unlikely that this process is important for Caloris because it is not obvious that the basin fill is free to contract horizontally and because it is unlikely that the compressional features are as shallow as the theory requires.

For a basin initially in isostatic equilibrium which then has a thickness of material b added on top, it can be shown that the original floor subsides by an amount $b\rho_b/\rho_m$, where ρ_b and ρ_m are the densities of the added material and the mantle respectively. This subsidence is reduced if the elastic strength of the lithosphere is significant at the basin length-scale. Thus, to cause the inferred strains would probably require >5 km of fill material to the basin interior. This is a large amount of volcanism; for instance, estimated thicknesses of mare fill on the Moon range from 0.5 to 4.7 km (Williams and Zuber, 1998). It is, therefore, not yet clear whether subsidence alone can explain the observed wrinkle ridges. The apparent age of many of the known compressional tectonic features on Mercury suggests the Caloris wrinkle ridges formed at about the same time as wrinkle ridges and lobate scarp thrust faults in the smooth plains and intercrater plains (Watters *et al.*, 2004, 2005). A combination of subsidence and compressional stresses due to global contraction could account for the Caloris wrinkle ridges.

Loads which are partially rigidly supported produce positive gravity anomalies which can lead to reorientation of the planet; Murray *et al.* (1974) suggested that the present-day location of Caloris might be due to such a gravity anomaly. If the wrinkle ridges are evidence for subsidence, as seems likely, then it is important to examine whether the inferred subsidence and fill thickness are consistent with the predicted gravity anomaly. We discuss this issue below (Section 4.4).

4.3.2 Extensional troughs, exterior loading, and lateral crustal flow

The existence of radial and concentric graben that postdate the wrinkle ridges is puzzling, especially in view of the fact that similar features are not observed in mascons on the Moon. It is clear that a mascon tectonic model cannot account for the spatial and temporal distribution of tectonic features in Caloris. Thomas

et al. (1988) suggested that inward motion towards Caloris caused updoming and extension. Melosh and McKinnon (1988) advocated exterior, annular loading of the Caloris basin causing basin interior uplift. This model invokes an annular load extending 650 to 1800 km radial distance from the basin center (Melosh, 1978) with a T_e from 75 km to 125 km (McKinnon, 1986). The Thomas *et al.* (1988) model does not really explain why similar features are not seen in similar basins on the Moon or Mars; while the Melosh and McKinnon (1988) basin exterior loading model depends on the poorly known thickness of the circum-Caloris deposits. A third possibility is that the Caloris graben are due to thermal contraction or subsurface heating of near-surface volcanic plains, as has been proposed for Venus (Johnson and Sandwell, 1992); however, both these explanations are problematic. Surface cooling is unlikely to produce features of the scale observed, while subsurface heating is not only ad hoc but also disagrees with the observations.

The Caloris graben may also be explained by lateral crustal flow (Watters *et al.*, 2005). After the formation of an impact basin pressure gradients exist that can drive flow in the lower crust, even if the crust is isostatically compensated. This lateral flow of the lower crust will result in uplift of the existing basin materials and occurs at a rate determined by the crustal thickness, rheology, and thermal gradient. The rate of flow is always much slower than the vertical mantle motion discussed above (Zhong, 1997; McKenzie *et al.*, 2000) but can still be significant. If such lateral flow does occur, the result is uplift by an amount depending on the initial thinning of the crust and the lithospheric rigidity. Although the topography of Caloris is currently not well determined, the basin is clearly relatively shallow (e.g., Schaber *et al.*, 1977), and thus uplift due to lateral crustal flow is very likely to have occurred. Melosh and McKinnon (1988) note that domical uplift would likely lead to radial graben, while a mix of radial and concentric graben is actually observed. An extensional strain of roughly 0.08% requires an uplift of about 3 km for $T_e = 30$ km, $w_0 \sim 1$ km for $T_e = 100$ km, and $w_0 < 1$ km for $T_e = 150$ km (Equation 2.3).

Lateral crustal flow causes thickening of the crust beneath the impact basin, which in turn generates uplift and extension (Watters *et al.*, 2005, Fig. 4). As lower crustal flow proceeds, uplift leads to extensional stresses. The main controls on the amount of lower crustal flow are heat flux, crustal thickness, and rheology. The degree of lower crustal flow can be parameterized by the basin relaxation, defined as the ratio of basin uplift:initial depth. If the heat flux is set by the likely radiogenic values, then for the assumed rheology, a crustal thickness of 90 to 140 km is required (Watters *et al.*, 2005). This derived range in crustal thickness is consistent with other estimates (see Section 3.2).

The maximum extensional stress occurs away from the basin center because Watters *et al.* (2005) assumed a flat-floored initial basin geometry. This geometry is

in agreement with recent studies of gravity anomalies associated with lunar mascons (Watters and Konopliv, 2001). An initially Gaussian-shaped basin results in stresses of the same magnitude but maximized at the basin center. The existence of a radial graben complex that converges near the center of Caloris (see Section 2.7), suggests that a combination of the two basin geometries, or preexisting fractures, may be needed to account for the basin-radial and basin-concentric graben.

Kennedy *et al.* (2008) evaluated both the external loading and the lateral flow models for a range of lithospheric structures using finite element analysis. In agreement with Melosh and McKinnon (1988), they found that the distribution of basin-interior graben can be accounted for by an annular load extending 750 to 1800 km radial distance from the basin center. To induce the necessary load, the basin exterior smooth plains must be thick, 5 km or more, so that extensional stresses from flexural uplift exceed compressional stresses due to subsidence of interior plains and global contraction. Kennedy *et al.* (2008) also conclude that infilling of the basin interior must have occurred in stages spaced over a period of time that exceeds the timescale for basin subsidence from a single interior load, to reduce compressional stresses in the uppermost layer of the plains material. In their analysis of the lateral crustal flow model, Kennedy *et al.* (2008) found that although basin-interior uplift will result from late-stage flow, the extensional stress patterns from lateral flow-induced uplift are not consistent with the observed distribution of graben imaged by Mariner 10.

MESSENGER's discovery of Pantheon Fossae is a critical new constraint on models for the origin of stresses in the Caloris basin. Both the exterior loading model and the lateral crustal flow model must be reevaluated to determine if they can account for the evolution of stresses necessary to explain the spatial and temporal distribution of wrinkle ridges and basin-radial and basin-concentric graben in Caloris. It is also unclear whether the external loading model is consistent with existing constraints from gravity on the mass of loading material present (see below).

4.4 Elastic thickness

Since Caloris is located on the approximate longitude (although not the latitude) of one of Mercury's principal axes of inertia, it has been suggested (Murray *et al.*, 1974) that it may possess a positive gravity anomaly – a mascon. Mascons are formed on the Moon by dense mare basalts flooding the basin after sufficient time has elapsed that the lithosphere is highly rigid (Solomon and Head, 1979; see Watters and Johnson, Chapter 4). Melosh and Dzurisin (1978b) used the location of Caloris to place a lower bound on the gravity anomaly and hence the local thickness of uncompensated lavas. Willemann (1984) pointed out that the fact that Caloris is not on the equator also places an upper bound on the thickness of the interior plains

material, though more recent work suggests that Willemann's (1984) theoretical approach is incomplete (Matsuyama *et al.*, 2006).

The models of Melosh and Dzurisin (1978b) and Willemann (1984) both used moment of inertia (MoI) values which were subsequently updated by Anderson *et al.* (1987). Furthermore, they assumed that the volcanic fill existed in an exterior annulus at a radial distance of 650 km to 1950 km from the center of the basin. Here we use the updated MoI and basin radius values, and also consider the effect of uncompensated volcanic fill forming a disk inside the basin (outer radius 775 km).

The revised upper bound (Anderson *et al.*, 1987) on J_2 of 8×10^{-5} gives an upper bound on the uncompensated exterior annular fill thickness of 1.8 km, slightly lower than the original Willemann (1984) estimate. If instead the volcanic fill forms a disk within the basin, the upper bound is 5.6 km. The lower bound on $(B - A)/C$ of 5×10^{-4} results in a lower bound on the annular fill thickness of 0.35 km, similar to the original Melosh and Dzurisin (1978b) estimate. The lower bound for the interior uncompensated fill thickness is 1.2 km. It should be noted that an upper limit on the uncompensated annular fill thickness of 1.8 km is significantly lower than the minimum thickness invoked by Kennedy *et al.* (2008) to account for the Caloris graben by exterior loading.

These results therefore suggest that roughly 1 km of annular uncompensated volcanic fill, or a few kilometers of uncompensated basin-filling volcanic material, can explain the position of Caloris. The actual thickness of the volcanic sequence could be much greater since wide loads will tend to be at least partially compensated. Basin fill thicknesses of >5 km were inferred above (Section 4.2) to explain trough and polygon widths and wrinkle-ridge strains. Thus, it appears that the basin fill is mostly, but not entirely compensated, which has implications for the elastic thickness of Caloris.

For a Cartesian situation, the degree to which a load of a particular wavelength is compensated, C, is given by (Turcotte and Schubert, 2002)

$$C = \frac{1}{1 + \dfrac{Dk^4}{\Delta\rho g}}, \quad D = \frac{ET_e^3}{12(1 - \nu^2)}, \tag{2.4}$$

where $0 \leq C \leq 1$, k is the wavenumber of the load, $\Delta\rho$ is the density contrast between mantle and crust, g is the acceleration due to gravity, D is the rigidity, E is the Young's modulus and ν is the Poisson's ratio. More complicated results exist for situations in which the curvature of the planet is important (e.g., Turcotte *et al.*, 1981; Willemann and Turcotte, 1982), but the basic dependence of the compensation factor on T_e remains the same. Assuming an effective load wavelength of 3100 km, values of C of 93%, 79% and 61% for T_e values of 100 km, 150 km and 200 km are obtained respectively. Since a mostly compensated situation is required

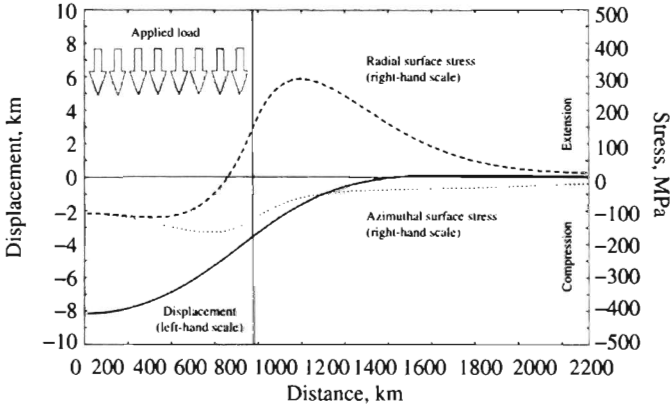

Figure 2.21. Displacement and stresses due to a radial load of 126 MPa (equivalent to a fill thickness of 10 km) and radius 775 km operating on an elastic shell with $T_e = 200$ km. Solid line is displacement, dotted line is surface azimuthal stress, dashed line is surface radial stress, arrows denote load, vertical line denotes edge of load. Values calculated using method of Solomon and Head (1979) using a planetary radius of 2440 km, Young's modulus of 100 GPa, Poisson's ratio 0.25, density 3400 kg m^{-3}, and gravity 3.7 m s^{-2}.

(C approaching 1) these results suggest that an elastic thickness on the order 100 km is appropriate.

A more precise estimate of T_e can be made by considering the case of a circular load imposed on a thin spherical shell. Figure 2.21 shows the deformation and stresses due to a load of radius 775 km on a shell with $T_e = 200$ km, calculated using the method of Solomon and Head (1979). The thickness of the load is 10 km if the load density is the same as that of the mantle (3400 kg m^{-3}); a higher density would result in a thinner load. The maximum subsidence is 8.2 km, indicating that the load is 82% compensated and the maximum compressional strain is of order 0.1%. The resulting gravity anomaly would be around 260 mGal. This model thus crudely agrees with both the geodetic constraints on the basin fill thickness and the requirements from the wrinkle-ridge strain estimates (Section 4.3). The same model with $T_e = 100$ km results in a load that is 99% compensated, inconsistent with the geodetic requirements. Thus, it appears that an elastic thickness of ~200 km is required to explain the Caloris observations. While this T_e estimate may appear large, similar values have been obtained for the lithosphere supporting the large Martian shield volcanoes (Zuber *et al.*, 2000).

4.5 Stresses

Figure 2.21 shows that substantial extensional stresses (~200 MPa) develop exterior to the basin. Circumferential grabens are observed on the margins of lunar

mascon basins, presumably in response to these extensional stresses. Solomon and Head (1979) showed that stresses of order 50 MPa were apparently enough to initiate lunar graben formation. Similar features have not been identified around the Caloris basin, as noted by Thomas *et al.* (1988) (see Section 2.7). The above calculations do not take into account sphericity, which may alter the resulting stresses somewhat (Janes and Melosh, 1990; Freed *et al.*, 2001). However, the relative magnitudes of the stresses for the Mercurian and lunar cases are unlikely to change, making the lack of observed grabens around Caloris puzzling. Possible explanations for their absence are: (1) the rock fracture strength is higher on Mercury; (2) the grabens do exist but have been buried by later resurfacing events; (3) the elastic thickness of Mercury's lithosphere prevented stresses from exceeding the rock strength; (4) the loading is sufficiently small that the fracture strength is not exceeded; (5) global compressional stresses reduced the local extensional stresses.

Possibility (1) seems unlikely; given that lunar rocks are likely at least as dry as rocks on Mercury, there seems little justification for assuming that their strengths are very different. Possibility (2) depends on whether volcanism exterior to Caloris postdated that of the interior. Crater density data indicates that the Caloris interior plains material may be older than the exterior annulus smooth plains material (Spudis and Guest, 1988, Table III; Strom *et al.*, 2008; Fassett *et al.*, 2009). Thus, it is unlikely that the exterior smooth plains material buried circumferential graben.

The stresses external to Caloris depend on both the elastic thickness and the amount of basin loading. Using the method of Solomon and Head (1979), the maximum extensional stress produced outside the Caloris basin as a function of basin fill thickness and lithospheric elastic thickness is shown in Figure 2.22. The location of this maximum stress point increases from $1.07\,R_0$ to $1.30\,R_0$ as T_e increases from 20 km to 200 km, where R_0 is the radius of the basin.

For a nominal rock strength of 50 MPa, Figure 2.22 shows that the basin fill thickness cannot exceed 1.7 km unless T_e exceeds 200 km. This fill estimate is substantially smaller than that derived from the wrinkle ridge observations. The basic problem is that the maximum compressional and extensional strains and stresses are always about the same (see Figure 2.21), and thus, if basin-interior compressional features are created, then it is likely that basin-exterior extensional features will also arise. The problem is exacerbated by the fact that crustal materials are generally weaker in tension than in compression, so lower stresses are required to produce high-angle normal faults rather than low-angle thrust faults (e.g. Turcotte and Schubert, 2002).

The most likely resolution of this problem is the possibility that global compressional stresses occurred simultaneously with the local loading stresses. A similar mechanism was advocated by Solomon and Head (1979) for the Moon. These global compressional stresses would have the effect of suppressing extensional

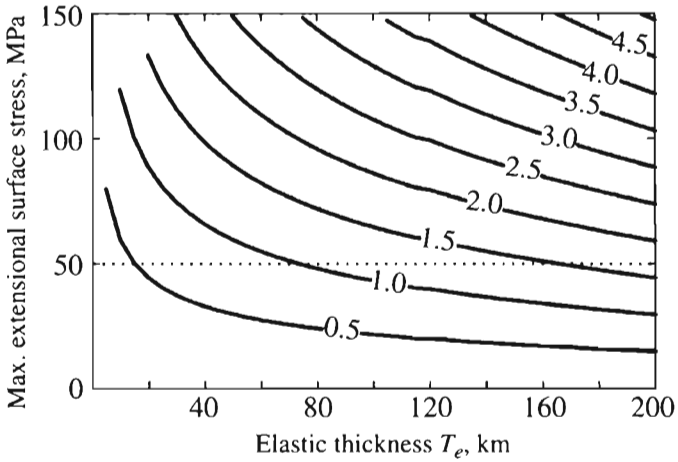

Figure 2.22. Maximum surface radial extensional stress as a function of fill thickness and elastic thickness. Load radius is 775 km, contours denote equivalent load thickness in kilometers, other parameters and method as in Figure 2.21. Dashed line denotes stress required to initiate extensional faulting on the Moon.

features and would thus permit thicker basin fills. As discussed below (Section 5.4), such stresses are likely to arise and can be comparable in magnitude to the flexural stresses discussed here.

4.6 Summary

The wrinkle ridges in Caloris are probably a result of subsidence due to infilling of the basin. This subsidence implies loading by a few to several tens of kilometers of basin fill material. Because Caloris is located at the longitude but not the latitude of one of Mercury's principal axes, both upper and lower limits can be placed on the thickness of uncompensated basin fill. Partially compensated loads can explain these constraints if the elastic thickness at the time of loading was ~150 to 200 km. The absence of circumferential graben about Caloris is probably because global contraction was occurring during basin loading and suppressed the formation of exterior extensional features. The interior extensional troughs, which overprint the wrinkle ridges, are probably due to subsequent uplift of the basin floor due to lateral crustal flow or basin-exterior loading.

5 Global implications

In the preceding sections, we have argued that the existence of lobate scarps and the characteristics of Caloris may be used to infer the properties of Mercury's crust and lithosphere. Here we investigate the pattern of deformation in the hemisphere

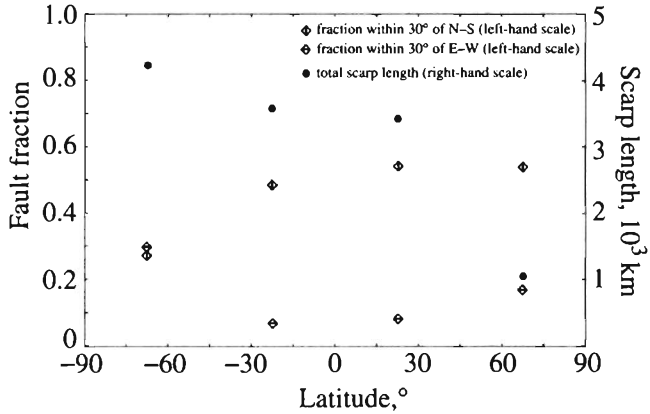

Figure 2.23. Lobate scarp orientations and distribution as a function of latitude. Diamonds indicate fraction of scarps within 30° of N–S or E–W orientations; contribution of each scarp segment is scaled by its length compared to the mean length. Circles indicate total length of scarps within each latitude bin. Mean orientations (standard deviations) of scarps within each latitude bin are (south to north): 45° (24°), 59° (19°), 60° (20°), 57° (22°).

imaged by Mariner 10 and the implications for the sources of stress and thermal evolution of the planet. As will become clear, a major difficulty in interpreting the different estimates of lithospheric properties is the poor understanding of both the relative and absolute timing of events.

5.1 Fault distribution

The distribution of orientations of lobate scarps mapped using Mariner 10 images is not uniform with latitude (see subsection 2.3.2). The fraction of lobate scarps which are within 30° of a N–S orientation and the fraction within 30° of an E–W direction as a function of latitude is shown in Figure 2.23. The plot was produced by combining mapped lobate scarp segments into longer straight line segments 20 to 30 km in length and obtaining the azimuth of each segment (see Section 2.2). The main trend is that equatorial lobate scarps are more likely to be N–S on average, while scarps at south latitudes have a stronger E–W component. The larger total length of lobate scarps towards the south pole is also evident (see Plate 1).

The predominance of N–S trending faults near the equator (Plate 1, Figure 2.23) is crudely consistent with the predictions of stresses caused by despinning (Melosh, 1977; Melosh and McKinnon, 1988, Fig. 3; Dombard and Hauck, 2008). However, the distribution of N–S trending lobate scarps imaged by Mariner 10 is not uniform across the equatorial zone (Plate 1), and the despinning model predicts no thrust faults in the mid-latitudes where lobate scarps are common (Watters *et al.*, 2004, Fig. 3). As explained below, the equatorial N–S thrust faults are diagnostic of

either a relatively thick lithosphere or an additional isotropic compressive stress. The main disagreement is that the despinning model predicts high-latitude E–W normal faults, while E–W thrust faults are actually observed. This could be the result of reactivation of preexisting normal faults, a well-known phenomenon on Earth. For instance, thrust faulting beneath the Zagros Mountains, Iran, occurs on relatively steeply dipping planes (30 to 60°) which are likely to be reactivated normal faults (Jackson, 1980). It is, therefore, possible that polar normal faults were generated by (extensional) despinning stresses and with continued contraction eventually led to these features being reactivated as thrust faults.

The fact that the greatest area-normalized cumulative length of lobate scarps occurs below 50°S in the Mariner 10 hemisphere (Watters *et al.*, 2004, Fig. 3) and that all the thrust faults in this region have the same fault-plane dip direction (Plate 1) is not easily explained by either tidal despinning or global thermal contraction. One possibility is that it may reflect some kind of preexisting structure, mechanical inhomogeneities, or variations in crustal thickness; another is some process similar to convective downwelling (Watters *et al.*, 2004) or mantle convection (King, 2008). Many lobate scarps in the hemisphere image by Mariner 10 have preferred orientations and thrust slip directions. New MESSENGER images of Mercury suggest that lobate scarps have a similar distribution with latitude as those imaged by Mariner 10 (see Solomon *et al.*, 2008; Watters *et al.*, 2009a,b). The global view to be provided by MESSENGER will reveal if there are other patterns in the spatial distribution, preferred orientations, and preferred thrust slip directions of the lobate scarps.

5.2 Rigidity

Evidence derived from the lobate scarps (Section 3.3) has been used to argue that T_e values on Mercury were quite modest (25 to 30 km). Conversely, the data for Caloris (Section 4.4) imply T_e values around 200 km and, as will be shown below, other authors have obtained comparable numbers. Since T_e is closely linked to heat flux, an understanding of these T_e variations is necessary when considering a planet's thermal evolution.

For planets such as Mars or Mercury which likely started hot, initial surface heat fluxes tend to exceed the radiogenic heat production (e.g., Nimmo and Stevenson, 2000). Although Mercury's complement of radiogenic elements is unknown, for bulk silicate Earth or bulk Moon abundances, the radiogenic heat flux at 4 Ga was about 30 mWm^{-2}. As long as radiogenic elements are not greatly concentrated in the near-surface (see Figure 2.20), the thermal gradient implied is about 10 K/km. Since this gradient neglects secular cooling, it is likely to be an underestimate. A likely upper bound on the base of the lithosphere is 1400 K, so the maximum

possible lithospheric thickness at 4 Ga is 100 km. As noted above (Section 3.2), much of the lithosphere retains little strength, so that the effective elastic thickness T_e is typically a factor of 3 to 4 lower than the lithospheric thickness. Thus, despite the uncertainties, our expectations of elastic thicknesses on Mercury at about 4 Ga are that they should be in the range 20 to 40 km. These expectations are consistent with the inferred BDT transition depth for the lobate scarps (see Section 3.2). However, they are inconsistent with other estimates, which we discuss below.

Melosh and McKinnon (1988) make three arguments that the elastic thickness of Mercury was ~100 km during the period of deformation. Firstly, the stresses which occur due to a despinning planet only lead to equatorial, N–S trending thrust faults if the elastic thickness exceeds about 0.05 of the planet's radius (Melosh, 1977). Since such faults are indeed observed, it was inferred that $T_e > 100$ km at the time of deformation. Secondly, the observed lack of multiring basins on Mercury was used to infer a T_e roughly greater than 100 km at the time of heavy bombardment. Finally, Melosh and McKinnon (1988) argued that the extensional faulting within Caloris could be explained by the emplacement of annular circum-Caloris plains materials. For such materials to cause the observed pattern of faulting requires a $T_e < 125$ km, while it was argued that faults would not form at all for a $T_e < 75$ km (the stresses would be too low).

Each of these constraints has its problems. For instance, even in a thin lithosphere, N–S trending faults can form at the equator if both contraction and despinning occur simultaneously (Pechmann and Melosh, 1979; Dombard and Hauck, 2008). Theoretical arguments and observations both suggest compressional stresses of comparable magnitudes to the despinning stresses (Sections 4.5, 5.4). Neither process has a well-constrained timescale, but both are likely to have been important in the first Gyr of Mercury's history. Dombard and Hauck (2008) examined despinning in combination with 3 to 5.5 km of global contraction before the end of the period of late heavy bombardment. The record of the resulting N–S oriented thrust faults is assumed to have been lost and the present population of lobate scarps is the expression of reactivated faults by later global contraction. Thus, the observed equatorial thrust faults are not necessarily evidence for a thick lithosphere. Similarly, simulations of the effects of large impacts on planetary lithospheres have only become available recently. Although such simulations can now be performed (e.g., Turtle and Pierazzo, 1998), the quantitative effect of lithospheric thickness on multiring basin formation is still unknown. Furthermore, strain rates during impacts are so different to strain rates of geological processes that the effective elastic thickness during an impact may be very different to that measured over geological timescales. Finally, as was argued above, an annular load may not be required to explain the extensional features within Caloris and it is not clear that the exterior plains materials are thick enough to generate the stresses required.

Nonetheless, despite the uncertainties, it seems likely that T_e during the formation of Caloris was ~100 km. Even higher values of T_e (~200 km) were obtained in Section 4.4 by considering the amount of subsidence required and the thickness of uncompensated basin fill. The disagreement between these two values is probably not significant, particularly in view of the fact that T_e may have varied over the course of the history of Caloris. For example, Solomon and Head (1979) found that T_e of the Serenitatis basin increased from 25 to 50 km at 3.8 to 3.6 Ga to ~100 km at 3.4 to 3.0 Ga. It is clearly important to understand the loading history of Caloris in more detail, both the order in which events occurred and the absolute durations of the events. Although as mentioned previously, crater density data suggest that there was a significant interval between the formation of the Caloris basin and the emplacement of the interior plains material (Spudis and Guest, 1988; Strom *et al.*, 2008; Fassett *et al.*, 2009), the absolute age of the two events is not well constrained.

There is a significant difference between the 100 to 200 km values of T_e obtained for Caloris and the 25 to 30 km values obtained from the lobate scarps (Section 3.3) and simple heat flux predictions. Since the lobate scarps generally appear to postdate the emplacement of the Calorian smooth plains (Spudis and Guest, 1988; Watters *et al.*, 2004), it is unlikely that Caloris loading occurred after the lobate scarps formed. Thus, the discrepancy cannot simply be due to an increase in T_e with time as expected for a cooling planet. One possibility is that Caloris is an area of thinned crust, resulting in a lithosphere containing more mantle material than usual. Since mantle material is intrinsically stronger than most crustal materials and contains fewer radiogenic elements, a thinned crust would likely lead to higher T_e values. Another possible explanation is that the lithospheric curvature associated with Caloris is much smaller than that of the short-wavelength scarps, resulting in a higher effective rigidity for the same thermal structure (cf. Watts, 2001). Regional variations in heat flux, either due to differing crustal concentrations (the lunar KREEP terrain; Wieczorek and Phillips, 2000) or mantle contributions, would need to have exceeded a factor of three to generate the T_e differences observed. None of these explanations is particularly satisfactory; the acquisition of gravity and topography data from the MESSENGER mission (Solomon *et al.*, 2001, 2007, 2008) will allow direct measurements of T_e and help to resolve some of these issues.

5.3 Amount of strain and contraction

While it is clear that Mercury has undergone global contraction, the amount of contraction is unclear. The amount of shortening and strain recorded by Mercury's lobate scarps has been used to estimate the global crustal shortening and radius change due to global contraction (Strom *et al.*, 1975; Watters *et al.*, 1998). Strom *et al.* (1975) estimated the horizontal shortening due to the lobate scarps by

assuming an average throw of 1 km and fault plane dips θ of 25° and 45°. The decrease in surface area expressed by the thrust faults was estimated by multiplying the average shortening by the total length of the lobate scarps mapped over an area covering ~24% of the surface. Extrapolating to the entire surface of Mercury, Strom *et al.* (1975) estimated a net decrease in area of up to 1.3×10^5 km^2. This corresponds to up to a 2 km decrease in the planet's radius (Strom *et al.*, 1975), consistent with thermal history models (Solomon, 1976; Schubert *et al.*, 1988).

The strain expressed by the lobate scarps can be determined using the *D–L* relationship of the faults (Equation 2.2) (Watters *et al.*, 1998). The lengths of the 82 mapped lobate scarps (Watters *et al.*, 2004) range from 36 km to 457 km, with a mean of 143 km and a standard deviation of 69 km. The longest lobate scarp in the hemisphere imaged by Mariner 10 is Discovery Rupes. Using the range of γ given in subsection 2.3.4 and the total length of the mapped lobate scarp fault segments (12 324 km), the areal strain is estimated to range from 0.035% to 0.053% (0.043% for $\theta = 30°$) for the 45% of the surface imaged by Mariner 10.

The radius change due to global contraction can be expressed by $\Delta R = R_d - \mathrm{R}_u$ where R_u is the pre-deformation planetary radius and R_d is the post-deformation (current) planetary radius. R_u is related to the contractional strain by

$$R_u = \left[\frac{R_d^2}{\varepsilon + 1}\right]^{0.5}. \tag{2.5}$$

Assuming the hemisphere imaged by Mariner 10 is representative of the entire surface, this range in ε corresponds to a range in ΔR of approximately -0.43 km to -0.64 km (-0.52 km for $\theta = 30°$). This amount of radius change is consistent with estimates by Watters *et al.* (1998) for a survey of lobate scarps over about 19% of the surface. Images obtained by MESSENGER showing lobate scarps in the hemisphere unseen by Mariner 10 and previously undetected lobate scarps in the Mariner 10 hemisphere, however, indicate that the above estimates of strain are too low. New estimates of the average contractional strain based on a survey of lobate scarps imaged by both MESSENGER and Mariner 10 are about one third greater (Solomon *et al.*, 2008) corresponding to a decrease in radius of up to 0.8 km (Watters *et al.*, 2009a).

Estimates of strain and radius change are critical to constraining thermal history models for Mercury (Solomon, 1976, 1977, 1978, 1979; Schubert *et al.*, 1988; Phillips and Solomon, 1997; Hauck *et al.*, 2004). Existing thermal history models predict much more radial contraction than can be accounted for with the observed tectonic features (on the order of 5 to 6 km) (Dombard *et al.*, 2001). Recent modeling suggests 1 to 2 km of radial contraction since 4 Ga can only be achieved with a bulk core sulfur content >6.5 wt% and a dry-olivine mantle rheology (Hauck *et al.*, 2004). Complete solidification of Mercury's core would result in a reduction

in planetary radius of about 17 km (Solomon 1976). However, core solidification may have begun before the crust was capable of recording any contraction. Thus, the observed lobate scarps only record the amount of planetary contraction that occurred after the period of late heavy bombardment and emplacement of the intercrater plains and thus likely only a fraction of the total contraction. The discrepancy between the observed and predicted strain has led to the suggestion that long-wavelength (>100 km), low-amplitude lithospheric folds, not visible in Mariner 10 images, may be present (Dombard *et al.*, 2001). Alternatively, since many of the known thrust faults do not appear to have formed prior to the emplacement of the youngest Calorian smooth plains, the strain recorded by the lobate scarps may represent only the last phase of planetary contraction.

On the Moon, global contraction is predicted on the basis of thermal evolution models, but lobate scarp thrust faults like those on Mercury are not observed (see Watters and Johnson, Chapter 4). Pritchard and Stevenson (2000) carried out a thorough investigation into this mismatch and concluded that it could be explained by: near-surface regolith being able to accommodate more contraction strain than intact rock before failing (e.g., Binder and Gunga, 1985); non-monotonic thermal evolution histories; or accommodation by numerous small faults (Weisberg and Hager, 1998). It is also likely that the crust can accommodate a small amount of elastic strain without undergoing observable brittle deformation. Any of these effects, including low-amplitude folds not detectable with the available data (Dombard *et al.*, 2001), could be important on Mercury. About all that can be said with certainty is that complete core solidification would produce more contraction than is observed and can be ruled out. This conclusion agrees with the observations of Peale (2003) and Margot *et al.* (2007) and new observations by MESSENGER (Solomon *et al.*, 2008) which suggest Mercury's core is at least partly liquid.

5.4 Sources of stress

5.4.1 Contraction

Both theoretical considerations and observations suggest that Mercury has undergone global contraction. The timing, duration, and magnitude of this contraction are unclear, but it seems likely that significant thermal contraction-related compressional stresses were present during the loading of Caloris (Section 4.5). The isotropic stresses σ resulting from global contraction (Melosh and McKinnon, 1988) are given by

$$\sigma = 2\mu \frac{(1+\nu)}{(1-\nu)} \frac{\Delta R}{R}, \tag{2.6}$$

where μ is the shear modulus, ν is the Poisson's ratio, R is the planetary radius, and ΔR is the radial contraction. A change in radius of 2 km gives rise to stresses

on the order of 100 MPa. If the upper limit of the radius change is on the order of 1 km (see Section 5.3), then the corresponding stresses are ~55 MPa (Watters *et al.*, 2000). This is comparable to the stresses derived from the inferred loading of the Caloris basin (Section 4.5).

5.4.2 Thermal stresses

Global thermal stresses arising from planetary cooling are closely related to planetary contraction. Models calculating vertically varying thermal stresses as the temperatures of the lithosphere and interior evolve have been constructed (e.g., Solomon and Head, 1979; Turcotte, 1983; Hauck *et al.*, 2004). The importance of these models is that in some circumstances they predict extension as well as compression. The magnitude of the stresses is given by equations of the form

$$\sigma = \alpha E \frac{\Delta T}{(1-\nu)}, \tag{2.7}$$

where σ is the thermal expansivity and ΔT is the temperature change. A temperature change of 100 K gives rise to stresses of order 300 MPa for a thermal expansivity of 3×10^{-5} K^{-1}.

Local thermal stresses may also arise due to cooling of volcanic plains, lithospheric reheating, or subsidence. While less important for global tectonic patterns, such stresses may be important in generating local features like polygonal troughs (Johnson and Sandwell, 1992).

5.4.3 Despinning

Observational arguments that despinning may have occurred are presented in Section 5.1. The maximum differential stress caused by despinning (Melosh and McKinnon, 1988; Matsuyama and Nimmo, 2009) is given by

$$\sigma = 5\left(\omega_1^2 - \omega_2^2\right)\frac{R^3}{GM}\mu\left(\frac{1+\nu}{5+\nu}\right), \tag{2.8}$$

where ω_1 and ω_2 are the initial and final angular rotation velocities, R is the planetary radius, M is the planetary mass, G is the gravitational constant, and μ is the shear modulus. If the initial spin period of Mercury was 20 hr, the stresses developed during despinning are of order 200 MPa, comparable to stresses due to contraction.

5.4.4 True polar wander

The discussion of Caloris suggests that the orientation of the planet's surface may have shifted with respect to its pole of rotation (Section 4.4). This reorientation causes the rotational bulge to change its position in relation to the surface and leads to lithospheric stresses (e.g., Melosh, 1980; Leith and McKinnon, 1996; Matsuyama

and Nimmo, 2009). The maximum differential stress σ which develops is given by (Melosh, 1980)

$$\sigma = \frac{4(1+\nu)}{(5+\nu)}\mu f \sin\theta, \tag{2.9}$$

where f is the planetary flattening at the time of reorientation, and θ is the angle of rotation.

Mercury's rotation is slow, and so the flattening would be expected to be small. Furthermore, radar altimetry data are restricted to an equatorial band, so the planetary flattening is poorly determined. The best estimate of f is 0.0029 ± 0.0036 (Anderson *et al.*, 1996) which is consistent with a value of zero. There is also a small equatorial ellipticity of $0.000\,54 \pm 0.000\,05$.

Taking $\mu = 40$ GPa, $\nu = 0.25$, and using $f = 0.003$ results in a differential stress of 20 MPa for a rotation of 10°. These stresses are not negligible compared with the other likely contributions if the flattening really is this large. However, detecting planetary reorientation through the spatial distribution of fractures is difficult (see Leith and McKinnon, 1996; Sarid *et al.*, 2002). Whether reorientation turns out to be an important effect will depend on better constraints on f and mapping of the global distribution of faults on Mercury.

5.4.5 Convection

Subsolidus mantle convection can potentially produce large stresses in the overlying lithosphere. These stresses depend on the temperature difference available to drive convection and for a strongly temperature-dependent viscosity (Solomatov and Moresi, 2000) are given by

$$\sigma \approx 0.03\alpha\rho g \Delta T_{rh} \delta_{rh}, \tag{2.10}$$

where σ is the thermal expansivity, ρ is the density, and ΔT_{rh} and δ_{rh} are the rheologically controlled temperature drop and boundary layer thickness. The value of δ_{rh} depends on the vigor of convection and is typically of order 100 km (see Solomatov and Moresi, 2000). The temperature contrast ΔT_{rh} for Newtonian rheologies is given by

$$\Delta T_{rh} \approx \frac{2.4RT_i^2}{Q}, \tag{2.11}$$

where R is the gas constant, T_i is the interior temperature, and Q is the activation energy. Assuming $Q = 250$ kJ/mol and $T_i = 1500$ K, we have $\Delta T_{rh} = 180$ K. The resulting stresses, from equation (2.10), are 6 MPa for a boundary layer thickness of 100 km. These stresses are small compared to the stresses arising due to other mechanisms.

Recent modeling, however, suggests that mantle convection may be an important source of tectonic stresses on Mercury. In three-dimensional convection simulations of Mercury's mantle, King (2008) found that a regularly spaced pattern developed. At low latitudes, mantle upwelling has a linear, sheet-like pattern creating dominantly E–W compression, while at the poles the pattern is almost hexagonal, creating generally N–S compression. These predicted stress patterns are roughly consistent with the orientations of the lobate scarps (see Plate 1). The modeled stresses are of the order of 500 MPa, which is much higher than the estimates derived from scaling arguments above, and in the absence of an elastic lithosphere would imply topographic variations with an amplitude of roughly 50 km. Further modeling is clearly required to resolve these issues.

5.4.6 Buoyancy forces

If isostatically compensated lateral crustal thickness contrasts exist, then buoyancy forces occur. The force (per unit length) (e.g., Buck, 1991) is given by

$$F \approx g \Delta\rho t_c \Delta t_c, \tag{2.12}$$

where $\Delta\rho$ is the density contrast between crust and mantle, and t_c and Δt_c are the mean crustal thickness and the thickness variation, respectively. If these forces are distributed uniformly across the entire crust, the stress is simply F/t_c. The stresses will be larger if they are confined to the elastic layer.

To produce a 1 km variation in elevation requires a Δt_c of about 6 km if $\Delta\rho = 500$ kg m^{-3}. The resulting buoyancy force is 10^{12} Nm^{-1} for a crustal thickness of 100 km. The mean stress across the entire crust is 10 MPa but may be higher if the stresses only occur within the elastic portion of the lithosphere. In any event, these stresses are probably small compared to other likely sources of stress.

5.5 Thermal evolution

Various authors have modeled the thermal evolution of Mercury with time (e.g., Schubert *et al.*, 1988; Spohn, 1991; Solomatov and Reese, 2001; Hauck *et al.*, 2004; Williams *et al.*, 2007). Unfortunately, there are essentially only two constraints at present. Firstly, the existence of a present-day magnetic field suggests an active dynamo, which in turn places constraints on the present-day core heat flux (Schubert *et al.*, 1988; Hauck *et al.*, 2004; Williams *et al.*, 2007). Secondly, the amount of global contraction places constraints on the total cooling. Understanding how T_e has varied with time would add an important constraint on thermal evolution, as it has for Mars (e.g., Zuber *et al.*, 2000).

Existing thermal evolution models leave many questions unanswered. For instance, it is not actually clear that mantle convection is required, especially if the material deforms in a non-Newtonian fashion (Solomatov and Reese, 2001). Similarly, the apparently plagioclase-rich crust is not likely to be generated by simple melting of mantle material, and perhaps implies an early magma ocean (cf. Wetherill, 1988) with little melt generation subsequently (Jeanloz *et al.*, 1995). This early event may have had important consequences for the transport of heat and radiogenic elements within Mercury. Finally, the recent discovery that Mercury's core is at least partially liquid (Peale, 2003; Margot *et al.*, 2007) has implications for the composition of the core and the cooling of the mantle.

5.6 Summary

The distribution of lobate scarps in the hemisphere imaged by Mariner 10 is not consistent with thrust faults formed during a despinning or thermal contraction episode alone. A combination of tidal despinning and thermal contraction may account for equatorial N–S and polar E–W trending lobate scarp thrust faults in the regions by reactivation of normal faults. These two mechanisms generate comparable stresses, probably occurred over similar timescales, and are likely to be important stress-generating mechanisms on Mercury. Nonetheless, they do not by themselves account for the spatial and temporal distribution of all lobate scarps. Another important source of stress that may account for the distribution and orientation of the lobate scarps is mantle convection. Local loading in the Caloris basin produced significant compressional stresses, similar in magnitude to those produced by despinning and thermal contraction (Section 4.5). The loading may also have led to planetary reorientation. Several lines of evidence suggest that T_e during Caloris loading was ~100 km. The role of polar wander-induced stresses is uncertain, while stresses due to crustal thickness variations are likely to be small. The amount of global contraction is at present poorly constrained, but estimates will be greatly improved by global high-resolution imaging obtained by MESSENGER.

6 Conclusions

Tectonic features on Mercury are dominantly compressional in origin. The most prominent tectonic landforms are the lobate scarp thrust faults found in the oldest (pre-Tolstojan) and youngest (Calorian) plains on Mercury. The lobate scarps are not uniformly distributed and have preferred orientations and fault-plane dip directions. Although the lobate scarps deform the oldest plains units, the scarcity of large, superimposed impact craters and their relatively undegraded appearance

suggest many formed after the emplacement of the youngest Calorian plains units. Wrinkle ridges are found exclusively in Calorian smooth plains units that generally occupy topographic lows, including the floor material of the Caloris basin. The wrinkle ridges in the Caloris basin form a circumferential pattern that is very similar to the pattern of wrinkle ridges found in lunar mascon basins. The Caloris basin is one of only three basins on Mercury with evidence of extensional deformation. Extension of the interior plains is expressed by a complex pattern of basin-radial and basin-concentric graben. The Caloris graben crosscut the wrinkle ridges and thus may be among the youngest tectonic features on Mercury.

Observations of tectonic features place constraints on geophysically important variables such as elastic thickness and heat flux. The lobate scarps provide constraints on T_e (~25 to 30 km), heat flux, and the amount of global contraction. Tidal despinning and planetary cooling and contraction are important sources of stress on Mercury, but by themselves or in combination do not account for all of the temporal and spatial distribution observed in the lobate scarp thrust faults. Local preferred orientations of the lobate scarps and uniform thrust slip dip directions suggest regional-scale stresses influenced the formation of the thrust faults. The wrinkle ridges in smooth plains outside of the Caloris basin are likely due to loading and subsidence of volcanic material that flooded lowland areas.

The wrinkle ridges in Caloris are probably due to subsidence following the infilling of the basin by volcanic material. The extensional polygonal troughs most likely result from either subsequent lateral crustal flow and uplift or basin-exterior loading. The absence of extensional features surrounding Caloris may be due to a background compressive stress resulting from global thermal contraction. Elastic thickness estimates based on Caloris structures imply $T_e \sim 100$ km, which is not consistent with estimates based on lobate scarp fault modeling. This mismatch cannot be explained by the lithosphere thickening with time, as Caloris formation appears to predate many of the lobate scarps. The explanation for this discrepancy is not currently obvious and will have to await the return of additional data from MESSENGER (Solomon *et al.*, 2001, 2007, 2008).

Acknowledgments

We wish to thank Jay Melosh and John Guest for their reviews and very helpful comments and suggestions that greatly improved this chapter. We also wish to thank Mark Robinson for providing Mariner 10 images and mosaics and for valuable insights into their processing and interpretation. The original version of this chapter was completed in April, 2006. This work was supported by the National Aeronautics

and Space Administration under Grants issued through the Office of the Planetary Geology and Geophysics Program.

References

Ackermann, R. V., Schlische, R. W., and Withjack, M. O. (2001). The geometric and statistical evolution of normal fault systems: An experimental study of the effects of mechanical layer thickness on scaling laws. *J. Struct. Geol.*, **23**, 1803–1819.

Anderson, J. D., Colombo, G., Esposito, P. B., Lau, E. L., and Tracer, G. B. (1987). The mass, gravity field and ephemeris of Mercury. *Icarus*, **71**, 337–349.

Anderson, J. D., Jurgens, R. F., Lau, E. L., and Slade, M. A. (1996). Shape and orientation of Mercury from radar ranging data. *Icarus*, **124**, 690–697.

André, S. L., Watters, T. R., and Robinson, M. S. (2005). The long wavelength topography of Beethoven and Tolstoj basins, Mercury. *Geophys. Res. Lett.*, **32**, L21202, doi:10.1029/2005GL023627.

Baldwin, R. B. (1963). *The Measure of the Moon*. Chicago, IL: University of Chicago Press.

Binder, A. B. (1982). Post-Imbrian global lunar tectonism: Evidence for an initially totally molten Moon. *Moon and the Planets*, **26**, 117–133.

Binder, A. B. and Gunga, H. C. (1985). Young thrust-fault scarps in the highlands: Evidence for an initially totally molten Moon. *Icarus*, **63**, 421–441.

Breuer, D., Spohn, T., and Wullner, U. (1993). Mantle differentiation and the crustal dichotomy of Mars. *Planet. Space Sci.*, **41**, 269–283.

Brewer, J. A., Smithson, S. B., Oliver, J. E., Kaufman, S., and Brown, L. D. (1980). The Laramide orogeny: Evidence from COCORP deep crustal seismic profiles in the Wind River mountains, Wyoming. *Tectonophysics*, **62**, 165–189.

Bryan, W. B. (1973). Wrinkle-ridges as deformed surface crust on ponded mare lava. *Geochim. Cosmochim. Acta*, **1**, (Suppl.), 93–106.

Buck, W. R. (1991). Modes of continental lithospheric extension. *J. Geophys. Res.*, **96**, 20 161–20 178.

Byerlee, J. (1978). Friction of rocks. *Pure Appl. Geophys.*, **116**, 615–626.

Cartwright, J. A., Trudgill, B. D., and Mansfield, C. S. (1995). Fault growth by segment linkage: An explanation for scatter in maximum displacement and trace length data from the Canyonlands grabens of SE Utah. *J. Struct. Geol.*, **17**, 1319–1326.

Cartwright, J. A., Mansfield, C. S., and Trudgill, B. D. (1996). The growth of normal faults by segment linkage. *Geol. Soc. Am. Spec. Publ.*, **99**, 163–177.

Clark, P. E., Leake, M. A., and Jurgens, R. F. (1988). Goldstone radar observations of Mercury. In *Mercury*, ed. F. Vilas, C. R. Chapman and M. S. Matthews. Tucson, AZ: University of Arizona Press.

Clark, R. and Cox, S. (1996). A modern regression approach to determining fault displacement-length scaling relationships. *J. Struct. Geol.*, **18**, 147–154.

Cook, A. C. and Robinson, M. S. (2000). Mariner 10 stereo image coverage of Mercury. *J. Geophys. Res.*, **105**, 9429–9443.

Cordell, B. M. and Strom, R. G. (1977). Global tectonics of Mercury and the Moon. *Phys. Earth Planet. Inter.*, **15**, 146–155.

Cowie, P. A. and Scholz, C. H. (1992a). Physical explanation for the displacement–length relationship of faults using a post-yield fracture-mechanics model. *J. Struct. Geol.*, **14**, 1133–1148.

Cowie, P. A. and Scholz, C. H. (1992b). Displacement-length scaling relationship for faults data synthesis and discussion. *J. Struct. Geol.*, **14**, 1149–1156.
Cowie, P. A. and Shipton, Z. K. (1998). Fault tip displacement gradients and process zone dimensions. *J. Struct. Geol.*, **20**, 983–997.
Cowie, P. A., Scholz, C. H., Edwards, M., and Malinverno, A. (1993). Fault strain and seismic coupling on mid-ocean ridges. *J. Geophys. Res.*, **98**, 17 911–17 920.
Davis, P. A. and Soderblom, L. A. (1984). Modeling crater topography and albedo from monoscopic Viking Orbiter images. *Icarus*, **89**, 9449–9457.
Dawers, N. H. and Anders, M. H. (1995). Displacement-length scaling and fault linkage. *J. Struct. Geol.*, **17**, 607–614.
Dawers, N. H., Anders, M. H., and Scholz, C. H. (1993). Growth of normal faults: displacement length scaling. *Geology*, **21**, 1107–1110.
Denevi, B. W., Robinson, M. S., Solomon, S. C., Murchie, S. L., Blewett, D. T., Domingue, D. L, McCoy, T. J., Ernst, E. M., Head, J. W., Watters, T. R., and Chabot, N. L. (2009). The evolution of Mercury's crust: A global perspective from MESSENGER. *Science*, **324**, 613–618.
Dombard, A. J. and Hauck, S. A. (2008). Despinning plus global contraction and the orientation of lobate scarps on Mercury. *Icarus*, **198**, 274–276.
Dombard, A. J., Hauck, S. A., Solomon, S. C., and Phillips, R. J. (2001). Potential for long-wavelength folding on Mercury (abs.). *Lunar Planet. Sci. Conf. XXXII*, 2035.
Dzurisin, D. (1978). The tectonic and volcanic history of Mercury as inferred from studies of scarps, ridges, troughs, and other lineaments. *J. Geophys. Res.*, **83**, 4883–4906.
Fisher, N. I. (1993). *Statistical Analysis of Circular Data*. Cambridge: Cambridge University Press, p. 277.
Foster, A. and Nimmo, F. (1996). Comparisons between the rift systems of East Africa, Earth, and Beta Regio, Venus. *Earth Planet. Sci. Lett.*, **143**, 183–195.
Freed, A. M., Melosh, H. J., and Solomon, S. C. (2001). Tectonics of mascon loading: Resolution of the strike-slip faulting paradox. *J. Geophys. Res.*, **106**, 20 603–20 620.
Gillespie, P. A., Walsh, J. J., and Watterson, J. (1992). Limitations of dimension and displacement data from single faults and the consequences for data analysis and interpretation. *J. Struct. Geol.*, **14**, 1157–1172.
Golombek, M. P. (1979). Structural analysis of lunar grabens and the shallow crustal structure of the Moon. *J. Geophys. Res.*, **84**, 4657–4666.
Golombek, M. P., Plescia, J. B., and Franklin, B. J. (1991). Faulting and folding in the formation of planetary wrinkle ridges. *Proc. Lunar Planet. Sci. Conf. 21*, 679–693.
Golombek, M. P., Anderson, F. S., and Zuber, M. T. (2001). Martian wrinkle ridge topography: Evidence for subsurface faults from MOLA. *J. Geophys. Res.*, **106**, 23 811–23 821.
Gries, R. (1983). Oil and gas prospecting beneath Precambrian of foreland thrust plates in Rocky Mountains. *Am. Assoc. Petrol. Geol. Bull.*, **67**, 1–28.
Hapke, B., Danielson, E., Klaasen, K., and Wilson, L. (1975). Photometric observations of Mercury from Mariner 10. *J. Geophys. Res.*, **80**, 2431–2443.
Hardacre, K. M. and Cowie, P. A. (2003). Controls on strain localization in a two-dimensional elastoplastic layer: Insights into size-frequency scaling of extensional fault populations. *J. Geophys. Res.*, **108**, 2529.
Harmon, J. K. and Campbell, D. B. (1988). Radar observations of Mercury. In *Mercury*, ed. F. Vilas, C. R. Chapman and M. S. Matthews. Tucson, AZ: University of Arizona Press, pp. 101–117.
Harmon, J. K., Campbell, D. B., Bindschadler, K. L., Head, J. W., and Shapiro, I. I. (1986). Radar altimetry of Mercury: A preliminary analysis. *J. Geophys. Res.*, **91**, 385–401.

Hauck, S. A., Dombard, A. J., Phillips, R. J., and Solomon, S. C. (2004). Internal and tectonic evolution of Mercury. *Earth Planet. Sci. Lett.*, **222**, 713–728.

Hawkins, S. E., Boldt, J., Darlington, E. H., Espiritu, R., Gold, R., Gotwols, B., Grey, M., Hash, C., Hayes, J., Jaskulek, S., Kardian, C., Keller, M., Malaret, E., Murchie, S. L., Murphy, P., Peacock, K., Prockter, L., Reiter, A., Robinson, M. S., Schaefer, E., Shelton, R., Sterner, R., Taylor, H., Watters, T., and Williams, B. (2007). The Mercury Dual Imaging System (MDIS) on the MESSENGER spacecraft. *Space Sci. Rev.*, **131**, 247–338.

Head, J. W., Murchie, S. L., Prockter, L. M., Robinson, M. S., Solomon, S. C., Strom, R. G., Chapman, C. R., Watters, T. R., McClintock, W. E., Blewett, D. T., and Gillis-Davis, J. J. (2008). Volcanism on Mercury: Evidence from the first MESSENGER flyby. *Science*, **321**, 69–72.

Hiesinger, H. and Head, J. W. (2000). Characteristics and origin of polygonal terrain in southern Utopia Planitia, Mars: Results from Mars Orbiter Laser Altimeter and Mars Orbiter Camera Data. *J. Geophys. Res.*, **105**, 11 999–12 022.

Howard, K. A. and Muehlberger, W. R. (1973). Lunar thrust faults in the Taurus-Littrow region. *Apollo 17 Prel. Sci. Rep., NASA Spec. Publ.*, **SP-330**, 31–22 – 31–25.

Jackson, J. A. (1980). Reactivation of basement faults and crustal shortening in orogenic belts. *Nature*, **283**, 343–346.

Jaeger, J. C. and Cook, N. G. W. (1979). *Fundamentals of Rock Mechanics*, 3rd edn. London: Chapman and Hall, p. 593.

Janes, D. M. and Melosh, H. J. (1990). Tectonics of planetary loading: A general model and results. *J. Geophys. Res.*, **95**, 21 345–21 355.

Jeanloz, R., Mitchell, D. L., Sprague, A. L., and DePater, I. (1995). Evidence for a basalt-free surface on Mercury and implications for internal heat. *Science*, **268**, 1455–1457.

Johnson, C. L. and Sandwell, D. T. (1992). Joints in Venusian lava flows. *J. Geophys. Res.*, **97**, 13 601–13 610.

Kennedy, P. J., Freed, A. M., and Solomon, S. C. (2008). Mechanisms of faulting in and around Caloris basin, Mercury. *J. Geophys. Res.*, **113**, E08004, doi:10.1029/2007JE002992.

King, S. D. (2008). Pattern of lobate scarps on Mercury's surface reproduced by a model of mantle convection. *Nature Geoscience*, **1**, 229–232.

Kirk, R. L., Barrett, J. M., and Soderblom, L. A. (2003). Photoclinometry made simple . . . ? In *Advances in Planetary Mapping 2003*. Houston, TX: Lunar and Planetary Institute.

Leith, A. C. and McKinnon, W. B. (1996). Is there evidence for polar wander on Europa? *Icarus*, **120**, 387–398.

Lucchitta, B. K. (1976). Mare ridges and related highland scarps: Results of vertical tectonism. *Geochim. Cosmochim. Acta*, **3**, (Suppl.), 2761–2782.

Maggi, A., Jackson, J. A., McKenzie D., and Priestley K. (2000). Earthquake focal depths, effective elastic thickness, and the strength of the continental lithosphere. *Geology*, **28**, 495–498.

Malin, M. C. (1976). Observations of intercrater plains on Mercury. *Geophys. Res. Lett.*, **3**, 581–584.

Malin, M. C. and Dzurisin, D. (1977). Landform degradation on Mercury, the Moon, and Mars: Evidence from crater depth/diameter relationships. *J. Geophys. Res.*, **82**, 376–388.

Margot, J. L., Peale, S. J., Jurgens, R. F., Slade, M. A., and Holin, I. V. (2007). Large longitude libration of Mercury reveals a molten core. *Science*, **316**, 710–714.

Marrett, R. and Allmendinger, R. W. (1991). Estimates of strain due to brittle faulting: Sampling of fault populations. *J. Struct. Geol.*, **13**, 735–738.

Matsuyama, I. and Nimmo, F. (2009). Gravity and tectonic patterns of Mercury: The effect of tidal deformation, spin-orbit resonance, non-zero eccentricity, despinning and reorientation. *J. Geophys. Res.*, **114**, E01010.

Matsuyama, I., Mitrovica, J. X., Manga, M., Perron, J. T., and Richards, M. A. (2006). Rotational stability of dynamic planets with elastic lithospheres. *J. Geophys. Res.*, **111**, E2, E02003.

Maxwell, T. A. and Gifford, A. W. (1980). Ridge systems of Caloris: Comparison with lunar basins. *Proc. Lunar Planet. Sci. Conf. 11*, 2447–2462.

Maxwell, T. A., El-Baz, F., and Ward, S. W. (1975). Distribution, morphology, and origin of ridges and arches in Mare Serenitatis. *Geol. Soc. Am. Bull.*, **86**, 1273–1278.

McEwen, A. S. (1991). Photometric functions for photoclinometry and other applications. *Icarus*, **92**, 298–311.

McGill, G. E. (1971). Attitude of fractures bounding straight and arcuate lunar rilles. *Icarus*, **14**, 53–58.

McGill, G. E. (1986). The giant polygons of Utopia, northern Martian plains. *Geophys. Res. Lett.*, **13**, 705–708.

McKenzie, D., Nimmo, F., Jackson, J. A., Gans, P. B., and Miller, E. L. (2000). Characteristics and consequences of flow in the lower crust. *J. Geophys. Res.*, **105**, 11 029–11 046.

McKinnon, W. B. (1980). Large impact craters and basins: Mechanics of syngenetic and postgenetic modification. Ph.D. thesis, California Institute of Technology.

McKinnon, W. B. (1986). Tectonics of the Caloris basin, Mercury (abs.). In *Mercury: Program and Abstracts*. Tucson, AZ: Div. Planet. Sci., Amer. Astron. Soc.

McNutt, M. K. (1984). Lithospheric flexure and thermal anomalies. *J. Geophys. Res.*, **89**, 1180–1194.

Mege, D. and Reidel, S. P. (2001). A method for estimating 2D wrinkle ridge strain from application of fault displacement scaling to the Yakima folds, Washington. *Geophys. Res. Lett.*, **28**, 3545–3548.

Melosh, H. J. (1977). Global tectonics of a despun planet. *Icarus*, **31**, 221–243.

Melosh, H. J. (1978). The tectonics of mascon loading. *Proc. Lunar Planet. Sci. Conf. 9*, 3513–3525.

Melosh, H. J. (1980). Tectonic patterns on a tidally distorted planet. *Icarus*, **43**, 454–471.

Melosh, H. J. (1989). *Impact Cratering: A Geologic Process.* Oxford Monographs on Geology and Geophysics, No. 11. New York, NY: Oxford University Press, p. 245.

Melosh, H. J. and Dzurisin, D. (1978a). Mercurian global tectonics: A consequence of tidal despinning? *Icarus*, **35**, 227–236.

Melosh, H. J. and Dzurisin, D. (1978b). Tectonic implications for gravity structure of Caloris basin, Mercury. *Icarus*, **33**, 141–144.

Melosh, H. J. and McKinnon, W. B. (1988). The tectonics of Mercury. In *Mercury*, ed. F. Vilas, C. R. Chapman and M. S. Matthews. Tucson, AZ: University of Arizona Press.

Montesi, L. G. J. and Zuber, M. T. (2003a). Spacing of faults at the scale of the lithosphere and localization instability: 1. Theory. *J. Geophys. Res.*, **108**, 2110.

Montesi, L. G. J. and Zuber, M. T. (2003b). Spacing of faults at the scale of the lithosphere and localization instability: 2. Application to the Central Indian Basin. *J. Geophys. Res.*, **108**, 2111.

Mouginis-Mark, P. J. and Wilson, L. (1981). MERC: A FORTRAN IV program for the production of topographic data for the planet Mercury. *Comput. Geosci.*, **7**, 35–45.

Murchie, S. L., Watters, T. R., Robinson, M. S., Head, J. W., Strom, R. G., Chapman, C. R., Solomon, S. C., McClintock, W. E., Prockter, L. M., Domingue, D. L., and Blewett, D. T. (2008). Geology of the Caloris Basin, Mercury: A new view from MESSENGER. *Science*, **321**, 73–76.

Murray, B. C., Belton, M. J. S., Danielson, G. E., Davies, M. E., Gault, D. E., Hapke, B., O'Leary, B., Strom, R. G., Suomi, V., and Trask, N. (1974). Mercury's surface: Preliminary description and interpretation from Mariner 10 pictures. *Science*, **185**, 169–179.

Nimmo, F. (2002). Constraining the crustal thickness of Mercury from viscous topographic relaxation. *Geophys. Res. Lett.*, **29**, 1063.

Nimmo, F. and Stevenson, D. J. (2000). Influence of early plate tectonics on the thermal evolution and magnetic field of Mars. *J. Geophys. Res.*, **105**, 11 969–11 979.

Nimmo, F. and Stevenson, D. J. (2001). Estimates of Martian crustal thickness from viscous relaxation of topography. *J. Geophys. Res.*, **106**, 5085–5098.

Nimmo, F. and Watters, T. R. (2004). Depth of faulting on Mercury: Implications for heat flux and crustal and effective elastic thickness. *Geophys. Res. Lett.*, **31**, L02701.

Parmentier, E. M. and Haxby, W. F. (1986). Thermal stresses in the oceanic lithosphere. Evidence from geoid anomalies at fracture zones. *J. Geophys. Res.*, **91**, 7193–7204.

Parsons, B. and McKenzie, D. (1978). Mantle convection and thermal structure of plates. *J. Geophys. Res.*, **93**, 4485–4496.

Peale, S. J. (2003). Mercury's interior from geodesy of librations (abs.). *Eos Trans. Am. Geophys. Union*, **84**(46), (Fall Meet. Suppl.), G42C-03.

Pechmann, J. B. (1980). The origin of polygonal troughs on the northern plains of Mars. *Icarus*, **42**, 185–210, doi:10.1016/0019-1035(80)90071-8.

Pechmann, J. B. and Melosh, H. J. (1979). Global fracture patterns of a despun planet application to Mercury. *Icarus*, **38**, 243–250.

Pike, R. J. (1988). Geomorphology of impact craters on Mercury. In *Mercury*, ed. F. Vilas, C. R. Chapman and M. S. Matthews. Tucson, AZ: University of Arizona Press, pp. 165–273.

Pike, R. J. and Spudis, P. D. (1987). Basin-ring spacing on the Moon, Mercury, and Mars. *Earth, Moon, and Planets*, **39**, 129–194.

Phillips, R. J. and Solomon, S. C. (1997). Compressional strain history of Mercury (abs.). *Lunar Planet. Sci. Conf. XXVIII*, 1107–1108.

Phillips, R. J., Conel, J. E., Abbott, E. A., Sjogren, W. L., and Morton, J. B. (1972). Mascons: Progress toward a unique solution for mass distribution. *J. Geophys. Res.*, **77**, 7106–7114.

Plescia, J. B. and Golombek, M. P. (1986). Origin of planetary wrinkle ridges based on the study of terrestrial analogs. *Geol. Soc. Am. Bull.*, **97**, 1289–1299.

Pritchard, M. E. and Stevenson, D. J. (2000). Thermal aspects of a lunar origin by giant impact. In *Origin of the Earth and Moon*, ed. R. Canup and K. Righter. Tucson, AZ: University of Arizona Press, pp. 179–196.

Reidel, S. P. (1984). The Saddle Mountains: The evolution of an anticline in the Yakima fold belt. *Am. Jour. Sci.*, **284**, 942–978.

Rice, J. R. (1992). Fault stress states, pore pressure distributions and the weakness of the San Andreas fault. In *Fault Mechanics and Transport Properties of Rocks*, ed. B. Evans and T.-F. Wong. San Diego: Academic Press, pp. 475–503.

Robinson, M. S. and Lucey, P. G. (1997). Recalibrated Mariner 10 color mosaics: Implications for Mercurian volcanism. *Science*, **275**, 197–200.

Robinson, M. S., Davies, M. E., Colvin, T. R., and Edwards, K. E. (1999). A revised control network for Mercury. *J. Geophys. Res.*, **104**, 30 847–30 852.

Robinson, M. A., Murchie, S. L., Blewett, D. T., Domingue, D. L., Hawkins, S. E., Head, J. W., Holsclaw, G. M., McClintock, W. E., McCoy, T. J., McNutt, R. L., Prockter, L. M., Solomon, S. C., and Watters, T. R. (2008). Reflectance and color variations on Mercury: Indicators of regolith processes and compositional heterogeneity. *Science*, **321**, 66–69.

Sarid, A. R., Greenberg, R., Hoppa, G. V., Hurford, T. A., Tufts, B. R., and Geissler, P. (2002). Polar wander and surface convergence of Europa's ice shell: Evidence from a survey of strike-slip displacement. *Icarus*, **158**, 24–41.

Schaber, G. G., Boyce, J. M., and Trask, N. J. (1977). Moon-Mercury large impact structures, isostasy and average crustal viscosity. *Phys. Earth Planet. Inter.*, **15**, 189–201.

Scholz, C. H. (2002). *The Mechanics of Earthquakes and Faulting*. Cambridge: Cambridge University Press, p. 471.

Scholz, C. H. and Cowie, P. A. (1990). Determination of total strain from faulting using slip measurements. *Nature*, **346**, 837–839.

Schubert, G., Ross, M. N., Stevenson, D. J., and Spohn, T. (1988). Mercury's thermal history and the generation of its magnetic field. In *Mercury*, ed. F. Vilas, C. R. Chapman and M. S. Matthews. Tucson, AZ: University of Arizona Press.

Schultz, R. A. (1997). Displacement-length scaling for terrestrial and Martian faults: Implications for Valles Marineris and shallow planetary grabens. *J. Geophys. Res.*, **102**, 12 009–12 015.

Schultz, R. A. (1999). Understanding the process of faulting: Selected challenges and opportunities at the edge of the 21st century. *J. Struct. Geol.*, **21**, 985–993.

Schultz, R. A. (2000). Localizaton of bedding-plane slip and backthrust faults above blind thrust faults: Keys to wrinkle ridge structure. *J. Geophys. Res.*, **105**, 12 035–12 052.

Schultz, R. A. and Fori, A. N. (1996). Fault-length statistics and implications of graben sets at Candor Mensa, Mars. *J. Struct. Geol.*, **18**, 272–383.

Schultz, R. A. and Fossen, H. (2002). Displacement-length scaling in three dimensions: The importance of aspect ratio and application to deformation bands. *J. Struct. Geol.*, **24**, 1389–1411.

Schultz, R. A. and Watters, T. R. (2001). Forward mechanical modeling of the Amenthes Rupes thrust fault on Mars. *Geophys. Res. Lett.*, **28**, 4659–4662.

Smrekar, S. E. and Phillips, R. J. (1991). Venusian highlands geoid to topography ratios and their implications. *Earth Planet. Sci. Lett.*, **107**, 582–597.

Smrekar, S. E., Moreels, P., and Franklin, B. J. (2002). Characterization and formation of polygonal fractures on Venus. *J. Geophys. Res.*, **107**, 8–1 – 8–18.

Solomatov, V. S. (1995). Scaling of temperature-dependent and stress-dependent viscosity convection. *Phys. Fluids*, **7**, 266–274.

Solomatov, V. S. and Moresi, L. N. (2000). Scaling of time-dependent stagnant lid convection: Application to small-scale convection on Earth and other terrestrial planets. *J. Geophys. Res.*, **105**, 21 795–21 817.

Solomatov, V. S. and Reese, C. C. (2001). Mantle convection and thermal evolution of Mercury revisited (abs.). In *Workshop on Mercury: Space Environment, Surface and Interior*. Houston, TX: Lunar and Planetary Institute, 1097, 92–95.

Solomon, S. C. (1976). Some aspects of core formation in Mercury. *Icarus*, **28**, 509–521.

Solomon, S. C. (1977). The relationship between crustal tectonics and internal evolution in the Moon and Mercury. *Phys. Earth Planet. Inter.*, **15**, 135–145.

Solomon, S. C. (1978). On volcanism and thermal tectonics on one-plate planets. *Geophys. Res. Lett.*, **5**, 461–464.

Solomon, S. C. (1979). Formation, history and energetics of cores in the terrestrial planets. *Phys. Earth Planet. Inter.*, **19**, 168–182.

Solomon, S. C. and Head, J. W. (1979). Vertical movement in mare basins: Relation to mare emplacement, basin tectonics and lunar thermal history. *J. Geophys. Res.*, **84**, 1667–1682.

Solomon, S. C. and Head, J. W. (1980). Lunar mascon basins: Lava filling, tectonics, and evolution of the lithosphere. *Rev. Geophys. Space Phys.*, **18**, 107–141.

Solomon, S. C., McNutt, R. L., Gold, R. E., Acuña, M. H., Baker, D. N., Boynton, W. V., Chapman, C. R., Cheng, A. F., Gloeckler, G., Head, J. W., Krimigis, S. M., McClintock, W. E., Murchie, S. L., Peale, S. J., Philips, R. J., Robinson, M. S., Slavin, J. A., Smith, D. E., Strom, R. G., Trombka, J. I., and Zuber, M. T. (2001). The MESSENGER mission to Mercury: Scientific objectives and implementation. *Planet. Space Sci.*, **49**, 1445–1465.

Solomon, S. C., McNutt, R. L., Gold, R. E., and Domingue, D. L. (2007). MESSENGER mission overview. *Space Sci. Rev.*, **131**, 3–39.

Solomon, S. C., McNutt, R. L., Watters, T. R., Lawrence, D. J., Feldman, W. C., Head, J. W., Krimigis, S. M., Murchie, S. L., Phillips, R. J., Slavin, J. A., and Zuber, M. T. (2008). Return to Mercury: A global perspective on MESSENGER's first Mercury flyby. *Science*, **321**, 59–62.

Spohn, T. (1991). Mantle differentiation and thermal evolution of Mars, Mercury and Venus. *Icarus*, **90**, 222–236.

Sprague, A. L., Nash, D. B., Witteborn, F. C., and Cruikshank, D. P. (1997). Mercury's feldspar connection: Mid-IR measurements suggest plagioclase. *Adv. Space Res.*, **19**, 1507–1510.

Spudis, P. D. and Guest, J. E. (1988). Stratigraphy and geologic history of Mercury. In *Mercury*, ed. F. Vilas, C. R. Chapman and M. S. Matthews. Tucson, AZ: University of Arizona Press.

Stone, D. S. (1985). Geologic interpretation of seismic profiles, Big Horn Basin, Wyoming: Part I. East Flank. In *Seismic Exploration of the Rocky Mountain Region*, ed. R. R. Gries and R. C. Dyer. Denver, CO: Rocky Mountain Association of Geologists, pp. 165–174.

Strom, R. G. (1972). Lunar mare ridges, rings and volcanic ring complexes. *Mod. Geol.*, **2**, 133–157.

Strom, R. G., Trask, N. J., and Guest, J. E. (1975). Tectonism and volcanism on Mercury. *J. Geophys. Res.*, **80**, 2478–2507.

Strom, R. G., Chapman, C. R., Merline, W. J., Solomon, S. C., and Head, J. W. (2008). Mercury cratering record viewed from MESSENGER's first flyby. *Science*, **321**, 79–81.

Tanaka, K. L. and Davis, P. A. (1988). Tectonic history of the Syria Planum province of Mars. *J. Geophys. Res.*, **93**, 14 893–14 907.

Thomas, P. G. (1997). Are there other tectonics than tidal despinning, global contraction and Caloris-related events on Mercury? A review of questions and problems. *Planet. Space Sci.*, **45**, 3–13.

Thomas, P. G., Masson, P., and Fleitout, L. (1988). Tectonic history of Mercury. In *Mercury*, ed. F. Vilas, C. R. Chapman and M. S. Matthews. Tucson, AZ: University of Arizona Press.

Turcotte, D. L. (1983). Thermal stresses in planetary elastic lithospheres (Proc. Lunar Planet. Sci. Conf. 13). *J. Geophys. Res.* (Suppl. 88), A585–A587.

Turcotte, D. L. and Schubert, G. (2002). *Geodynamics: Application of Continuum Physics to Geological Problems*. Cambridge: Cambridge University Press, p. 450.

Turcotte, D. L., Willemann, R. J., Haxby, W. F., and Norberry, J. (1981). Role of membrane stresses in the support of planetary topography. *J. Geophys. Res.*, **86**, 3951–3959.

Turtle, E. P. and Pierazzo, E. (1998). Constraints on the size of the Vredefort impact crater from numerical modeling. *Meteorit. Planet. Sci.*, **33**, 483–490.

Vilas, F. (1988). Surface composition of Mercury from reflectance spectrophotometry. In *Mercury*, ed. F. Vilas, C. R. Chapman and M. S. Matthews. Tucson, AZ: University of Arizona Press.

Walsh, J. and Watterson, J. (1988). Analysis of the relationship between displacements and dimensions of faults. *J. Struct. Geol.*, **10**, 239–247.

Watters, T. R. (1988). Wrinkle ridge assemblages on the terrestrial planets. *J. Geophys. Res.*, **93**, 10 236–10 254.

Watters, T. R. (1991). Origin of periodically spaced wrinkle ridges on the Tharsis plateau of Mars. *J. Geophys. Res.*, **96**, 15 599–15 616.

Watters, T. R. (1992). A system of tectonic features common to Earth, Mars and Venus. *Geology*, **20**, 609–612.

Watters, T. R. (1993). Compressional tectonism on Mars. *J. Geophys. Res.*, **98**, 17 049–17 060.

Watters, T. R. (2003). Thrust faulting along the dichotomy boundary in the eastern hemisphere of Mars. *J. Geophys. Res.*, **108** (E6), 5054, doi:10.1029/2002JE001934.

Watters, T. R. (2004). Elastic dislocation modeling of wrinkle ridges on Mars. *Icarus*, **171**, 284–294.

Watters, T. R. and Konopliv, A. S. (2001). The topography and gravity of Mare Serenitatis: Implications for subsidence of the mare surface. *Planet. Space Sci.*, **49**, 743–748.

Watters, T. R. and Robinson, M. S. (1997). Radar and photoclinometric studies of wrinkle ridges on Mars. *J. Geophys. Res.*, **102**, 10 889–10 903.

Watters, T. R. and Robinson, M. S. (1999). Lobate scarps and the origin of the Martian crustal dichotomy. *J. Geophys. Res.*, **104**, 18 981–18 990.

Watters, T. R., Robinson, M. S., and Cook, A. C. (1998). Topography of lobate scarps on Mercury: New constraints on the planet's contraction. *Geology*, **26**, 991–994.

Watters, T. R., Schultz, R. A., and Robinson, M. S. (2000). Displacement–length relations of thrust faults associated with lobate scarps on Mercury and Mars: Comparison with terrestrial faults. *Geophys. Res. Lett.*, **27**, 3659–3662.

Watters, T. R., Robinson, M. S., and Cook, A. C. (2001). Large-scale lobate scarps in the southern hemisphere of Mercury. *Planet. Space Sci.*, **49**, 1523–1530.

Watters, T. R., Schultz, R. A., Robinson, M. S., and Cook, A. C. (2002). The mechanical and thermal structure of Mercury's early lithosphere. *Geophys. Res. Lett.*, **29**, 1542.

Watters, T. R., Robinson, M. S., Bina, C. R., and Spudis, P. D. (2004). Thrust faults and the global contraction of Mercury. *Geophys. Res. Lett.*, **31**, L04071 doi:10.1029/2003GL019171.

Watters, T. R., Nimmo, F., and Robinson, M. S. (2005). Extensional troughs in the Caloris basin of Mercury: Evidence of lateral crustal flow. *Geology*, **33**, 669–672.

Watters, T. R., Solomon, S. C., Robinson, M. S., Head, J. W., André, S. L., Hauck, S. A., and Murchie, S. L. (2009a). The tectonics of Mercury: The view after MESSENGER'S first flyby. *Earth Planet. Sci. Lett.*, doi:10.1016/j.epsl.2009.01.025.

Watters, T. R., Head, J. W., Solomon, S. C., Robinson, M. S., Chapman, C. R., Denevi, B. W., Fassett, C. I., Murchie, S. L., and Strom, R. G. (2009b). Evolution of the Rembrandt impact basin on Mercury. *Science*, **324**, 618–621.

Watters, T. R., Murchie, S. L., Robinson, M. S., Solomon, S. C., Denevi, B. W., André, S. L., and Head, J. W. (2009c). Emplacement and tectonic deformation of smooth plains in the Caloris basin, Mercury. *Earth. Planet. Sci. Lett.*, doi:10.1016/j.epsl.2009.03.040.

Watts, A. B. (2001). *Isostasy and Flexure of the Lithosphere*. Cambridge: Cambridge University Press.

Weisberg, O. and Hager, B. H. (1998). Global lunar contraction with subdued surface topography. In *Origin of the Earth and Moon*, Proceedings of the Conference Held 1–3 December, 1998 in Monterey, California. Houston, TX: Lunar and Planetary Institute, p. 54.

Wetherill, G. W. (1988). Accumulation of Mercury from planetesimals. In *Mercury*, ed. F. Vilas, C. R. Chapman and M. S. Matthews. Tucson, AZ: University Arizona Press.

Wieczorek, M. A. and Phillips, R. J. (2000). The Procellarum KREEP Terrane: Implications for mare volcanism and lunar evolution. *J. Geophys. Res.*, **105**, 20 417–20 430.

Wilhelms, D. E. (1987). *The Geologic History of the Moon*. Washington, DC: U.S. Government Printing Office.

Willemann, R. J. (1984). Reorientation of planets with elastic lithospheres. *Icarus*, **60**, 701–709.

Willemann, R. J. and Turcotte, D. L. (1982). The role of lithospheric stress in the support of the Tharsis Rise. *J. Geophys. Res.*, **87**, 9793–9801.

Williams, J.-P., Aharonson, O., and Nimmo, F. (2007). Powering Mercury's dynamo. *Geophys. Res. Lett.*, **34**, L21201.

Williams, K. K. and Zuber, M. T. (1998). Measurement and analysis of lunar basin depths from Clementine altimetry. *Icarus*, **131**, 107–122.

Wojtal, S. F. (1996). Changes in fault displacement populations correlated to linkage between faults. *J. Struct. Geol.*, **18**, 265–279.

Zhong, S. (1997). Dynamics of crustal compensation and its influences on crustal isostasy. *J. Geophys. Res.*, **102**, 15 287–15 299.

Zuber, M. T. and Aist, L. L. (1990). The shallow structure of the Martian lithosphere in the vicinity of the ridged plains. *J. Geophys. Res.*, **95**, 14 215–14 230.

Zuber, M. T., Solomon, S. C., Philips, R. J., Smith, D. E., Tyler, G. L., Aharonson, O., Balmino, G., Banerdt, B. W., Head, J. W., Johnson, C. L., Lemoine, F. G., McGovern, P. J., Neumann, G. A., Rowlands, D. D., and Zhong, S. (2000). Internal structure and early thermal evolution of Mars from Mars Global Surveyor topography and gravity. *Science*, **287**, 1788–1793.